Mobility Modeling of Gallium Nitride Nanowires

by

Viswanathan Naveen Kumar

A Thesis Presented in Partial Fulfillment
of the Requirements for the Degree
Master of Science

Approved November 2017 by the
Graduate Supervisory Committee:

Dragica Vasileska, Chair
Yuji Zhao
Stephen Goodnick

ARIZONA STATE UNIVERSITY

December 2017

ABSTRACT

Semiconductor nanowires have the potential to emerge as the building blocks of next generation field-effect transistors, logic gates, solar cells and light emitting diodes. Use of Gallium Nitride (GaN) and other wide bandgap materials combines the advantages of III-nitrides along with the enhanced mobility offered by 2-dimensional confinement present in nanowires. The focus of this thesis is on developing a low field mobility model for a GaN nanowire using Ensemble Monte Carlo (EMC) techniques. A 2D Schrödinger-Poisson solver and a one-dimensional Monte Carlo solver is developed for an Aluminum Gallium Nitride/Gallium Nitride Heterostructure nanowire. A GaN/AlN/AlGaN heterostructure device is designed which creates 2-dimensional potential well for electrons. The nanowire is treated as a quasi-1D system in this work. A self-consistent 2D Schrödinger-Poisson solver is designed which determines the subband energies and the corresponding wavefunctions of the confined system. Three scattering mechanisms: acoustic phonon scattering, polar optical phonon scattering and piezoelectric scattering are considered to account for the electron phonon interactions in the system. Overlap integrals and 1D scattering rate expressions are derived for all the mechanisms listed. A generic one-dimensional Monte Carlo solver is also developed. Steady state results from the 1D Monte Carlo solver are extracted to determine the low field mobility of the GaN nanowires.

Dedicated to my parents and my dear brother, Anuj, for helping me start this journey

ACKNOWLEDGMENTS

I would begin by acknowledging Dr. Dragica Vasileska for her continuous guidance throughout my Masters study. Her mentorship was invaluable to the completion of my thesis.

I would also like to express my gratitude to Dr. Yuji Zhao and Dr. Stephen Goodnick for supervising this work as a part of my Graduate Committee.

My sincere thanks to all the members of my research group for providing valuable inputs to this work. I also wish to thank the school of Electrical, Computer and Energy Engineering at Arizona State University for providing me the opportunity to pursue my graduate studies.

I thank my parents, Mr. Viswanathan and Mrs. Nalini, and my brother Anuj, for their eternal support. I thank my friends, Shiladitya and Marut, for their continuous encouragement.

TABLE OF CONTENTS

CHAPTER Page

LIST OF TABLES

Table Page

LIST OF FIGURES

Figure Page

Figure Page

CHAPTER 1

NANOSCALE STRUCTURES AND TRANSPORT

1.1 Introduction to Nanowires

Quasi-two dimensional and quasi one-dimensional devices offer an interesting perspective into novel applications such as ballistic transport, high electron mobilities as well as interesting optoelectronic phenomena. Nanowires, in the strictest sense, are defined as a class of nanostructures with diameter in the tens of nanometers (for cylindrical nanowires) or a length to width ratio of 1000 (in the case of rectangular nanowires). Nanowires open huge possibilities in the field of Ultra Large Scale Integrated circuits(ULSI) since they can offer a large density of transistors for a relatively small chip area [1]. Semiconductor nanowires such as silicon nanowires and gallium nitride nanowires are increasingly finding applications in logic devices [2], optoelectronic devices such as light emitting diodes and lasers as well as photovoltaic devices. Nanowires are also being studied for their applications in Third Generation Photovoltaics [3].

Aside from silicon and the 'conventional' III-V materials like GaAs, wide bandgap materials like the III-Nitrides show promising potential for electronic and optoelectronic applications. 'Conventional' III-Vs are typically Phosphides and Arsenides [4], while wide bandgap and ultra-wide bandgap III-Vs are the Nitrides such as the GaN, AlN and InN material family. AlGaN alloys have excellent physical properties such as high breakdown fields, high electron mobilities and can be easily doped [5]. These large carrier mobilities make GaN nanowires perfect for FETs and logic devices. The morphology and size of GaN nanowires make them highly suitable for nanoscale devices and interconnects as well [6]. The properties of gallium nitride, such as direct band gap, high saturation velocity and

high thermal stability, make GaN nanowires ideal candidates. Ultrawide bandgap materials such as GaN and associated III-Nitride alloys also have large optical phonon energies which lead to observation of ballistic transport at room temperature and at larger voltages [7]. GaN nanowires have been grown by various methods including Chemical Vapor Deposition, Molecular Beam Epitaxy and Metal Organic Chemical Vapor Deposition [8]. Ballistic transport is one of the many uniquely observable phenomena in nanoscale structures [7]. In this transport regime, the electrons travel a distance larger than the mean free path without any scattering [7]. If there are no scattering events to impede the flow of electrons, it can lead to development of faster devices.

In [9], the authors observe ballistic transport in III-Nitride Heterostructures at room temperature. Since the optical phonon energy of these materials is very large compared to that of silicon ($\hbar\omega_{op}$ = 91.2 meV), this limits the polar optical phonon emission scattering events. This, coupled with the fact that GaN has mean free paths in the order of (<100nm), led the authors to observe quasi ballistic behavior nanoscale crosses as shown in Figure 1.

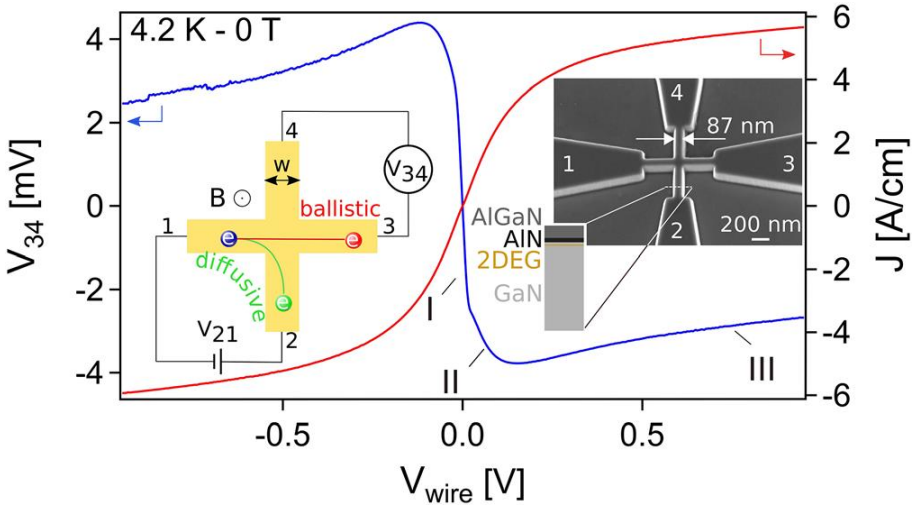

Figure 1.1 Nanowire crosses used to demonstrate ballistic transport by authors in [9]
Figure Courtesy of [9]

To comprehensively understand the transport phenomena in gallium nitride nanowires, it is necessary to characterize the confinement and the low field mobility of the nanostructure. Hence this work aims to develop a tool and simulate a “free standing” gallium nitride nanowire structure. A basic double gated AlGaN/AlN/GaN Heterostructure used by the authors in [9] is designed and simulated. In these structures, a 2-dimensional electron gas (2DEG) is induced at the AlN/GaN interface due to the strong polarization charges and additional confinement is achieved by the depletion regions created by the dual split gates. A 2D Schrödinger-Poisson solver is developed to determine the eigenstates and eigen-energies of the quasi-1D electron gas. The eigenfunctions and the subband energies are then fed into the 1 D Monte Carlo solver which simulates the 1D nanowire transport at low fields and outputs the electron mobility. As such, this solver will act as a precursor for future study onto lateral transport in complex nanowire structures.

The electron-phonon interactions are considered only in this study (phonon limited mobility). Specifically, we incorporate acoustic, polar optical phonon scattering and piezoelectric Scattering in the theoretical model. Electron-electron interactions and ionized impurity scattering are not considered as background doping in GaN nanowires is very low.

1.2 Device Design

To determine the mobility, an AlGaN/AlN/GaN heterostructure, like the one developed by the authors in [9] is simulated. In the experimental structure, a 200 nm thick GaN layer grown on a GaN substrate is followed by a strained layer of 8nm thick AlN. 20 nm thick AlGaN layer with an aluminum composition of 20% forms the top of the device. A double gated structure is created by placing metal contacts on top of the AlGaN layer leaving a

channel that is 87 nm wide. The same experimental device design is used for simulation in this work. Figure 1.2 shows the device structure along with dimensions and doping. The structure is double gated, leaving a channel in which the quasi 1D region exists. Confinement along the width (x-direction) of the device is ensured by putting a sufficiently high negative potential on the contacts in order to deplete the underlying regions. The doping of the top layers is kept high enough to create sufficient conduction band bending in the underlying GaN layer.

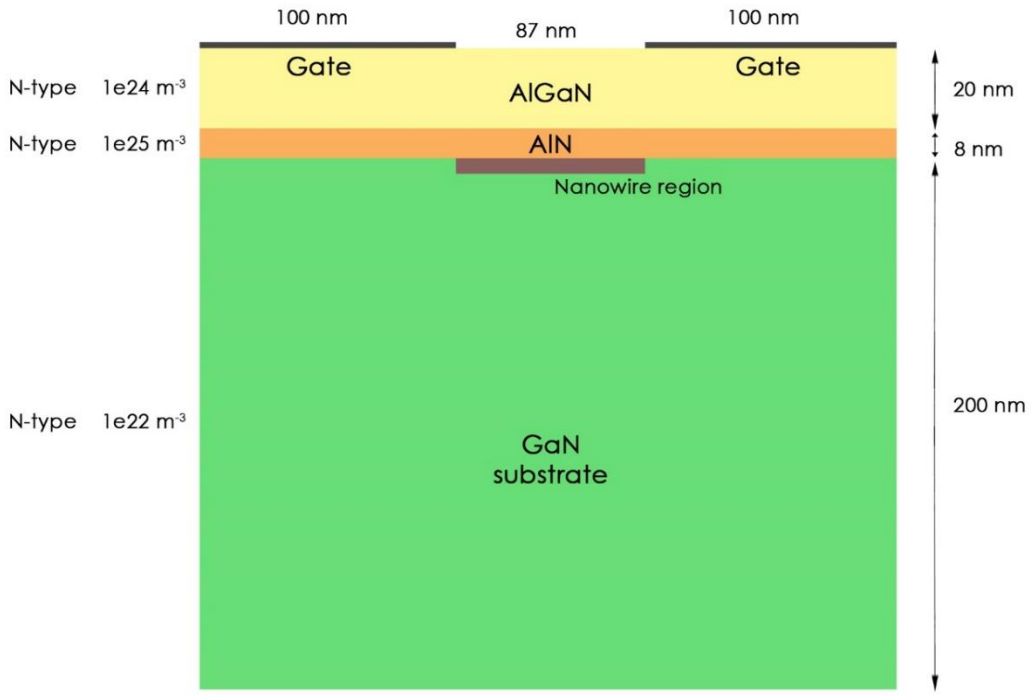

Figure 1.2 The design and dimensions of the dual gate AlGaN/AlN/GaN heterojunction device used in this work

As mentioned earlier, the dual gate structure is essential for 2-dimensional confinement. The conduction band bends below the fermi level at the GaN/AlN interface. A net positive charge is induced at the interface due to presence of spontaneous as well as piezoelectric

polarization. These factors lead to formation of a 2DEG at the interface and hence confinement along the depth (y) of the device.

1.3 Theory of Polarization charges

Group III-nitride materials naturally occur as a Wurtzite crystal structure with lattice constants a_0 and c_0 along the base hexagon and along the height respectively [10]. Since growth along the c plane {0001} is a highly mature standard, this discussion will be restricted to polarization in the c plane. The atoms are arranged in closely spaced hexagonal bilayers with alternating anion and cation layers creating a dipole moment. This forms the basis of spontaneous polarization present in the c plane of GaN. Depending on which atom is on the top surface, Ga-face or N- face crystals can be grown in [0001] and $[000\bar{1}]$ plane respectively [11].

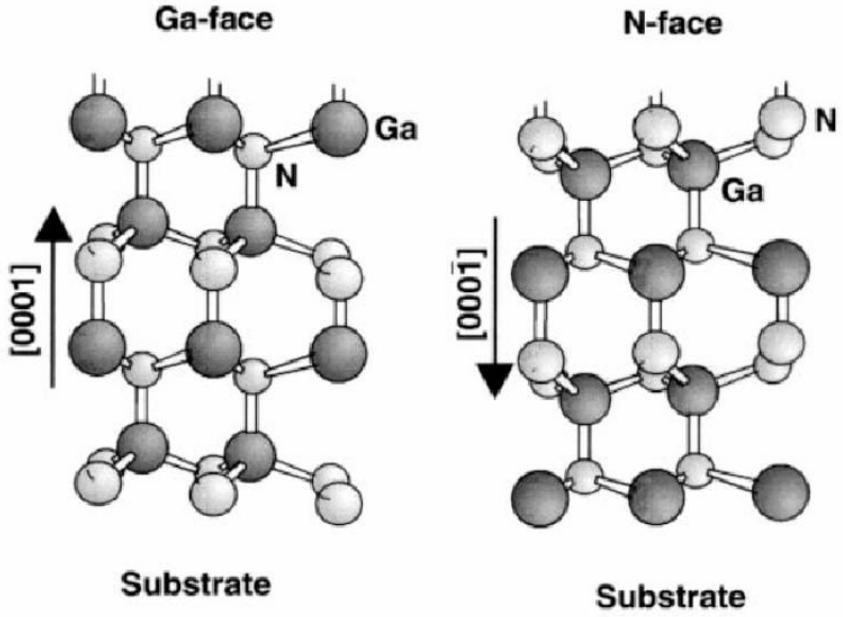

Figure 1.3 Gallium and Nitrogen faced Wurtzite crystals and their growth directions [11]

The spontaneous polarization in materials increases with increasing bond length. That is, with increasing cation-anion length, the spontaneous polarization (Psp) increases from GaN to AlN. Aside from spontaneous polarization, which is an inherent structural property of the material itself, piezoelectric polarization is also present in the strained layers. The total polarization charges present is the algebraic sum of spontaneous and piezoelectric polarization. Piezoelectric polarization along the c axis is given by the contribution of piezoelectric tensors and the in-plane and c-plane strain components. The relationship is given as [12]

$$Ppe = e33 * Ez + e31 * (Ex + Ey) \tag{1.1}$$

Where, e33 and e31 are piezoelectric coefficients and Ex, Ey and Ez are strain along the basal plane and c plane respectively.

The respective strain components are given by [12]

$$Ex = Ey = \frac{a - a0}{a0} \tag{1.2}$$

$$Ez = \frac{c - c0}{c0} \tag{1.3}$$

The unstrained lattice constants are given by a_0 and c_0, while a and c denote the lattice constants of the strained layer.

Using the relationship between lattice constants c and a in the GaN/AlN system[12],

$$\frac{c - c0}{c0} = -2\frac{C13}{C33}\frac{a - a0}{a0} \tag{1.4}$$

where, C13 and C33 are elastic constants. Thus, from equation (1.2) – (1.4) above, the expression for piezoelectric polarization is given as[12]

$$Ppe = \frac{2(a - a0)}{a0}\left(e31 - e33\frac{C13}{C33}\right) \quad (1.5)$$

For the AlGaN system, the second term in the above equation is always negative. Hence, the piezoelectric polarization is negative for tensile strain and positive for compressive strain. As mentioned earlier, the spontaneous polarization is also negative. Therefore, in the case of compressively strained AlGaN, the piezoelectric and spontaneous polarization are antiparallel to each other, while in the case of tensile strained layers, the spontaneous and piezoelectric polarization fields are parallel to each other. The net polarization charge at any interface is given by[12]

$$\sigma(Psp + Ppe) = P(bottom) - P(top) \quad (1.6)$$

For the device structure being considered, there are two abrupt interfaces; the AlN/GaN interface and AlGaN/AlN interface. Since the aluminum nitride and aluminum gallium nitride layers are under tensile strain, the piezoelectric and spontaneous polarization are parallel to each other. There is a net positive induced polarization charge at the AlN/GaN interface and hence free electrons from the GaN layer will populate the interface. This leads to the formation of a triangular well at the interface and a 2DEG, if the conduction band drops below the Fermi Level at the interface.

1.4 Formation of the 2 dimensional well and the 1D Density of States Function

The presence of AlGaN/AlN heterostructure causes the conduction band at the AlN/GaN interface to bend below the Fermi level. Along with the positive induced polarization charge at the interface, this causes electrons to be trapped in the triangular well. This is the

basis of confinement along the depth of the device. The aluminum composition as well as the doping and thickness of the layers can be adjusted to change the extent of band bending and, hence, alter the dimensions of the well.

Application of a negative potential at the dual gates present on the edges of the device causes depletion of electrons under the gates. This depletion layer forces the electron gas near the center of the device, with the peak electron density at the center of the nanowire just below the heterointerface. Effectively, this leads to formation of a square well along the width of the device and hence confinement of electrons along the (x) as well. Figures 1.4 and 1.5 describe the formation of the wells along the depth and the width of the device.

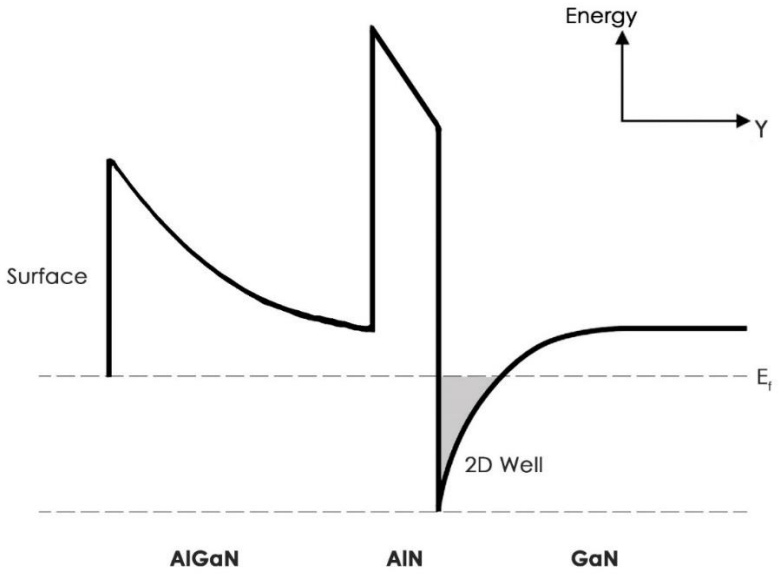

Figure 1.4 The triangular well obtained along the depth of the device. The 2D well region is shaded.

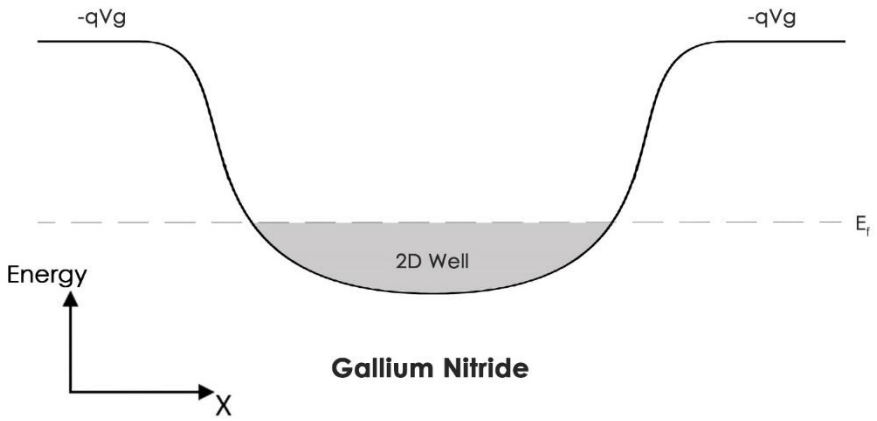

Figure 1.5 The square obtained along the x direction near the AlN/GaN interface upon application of Gate voltage -Vg. The 2D well region is shaded.

This so formed 2-dimensional confining potential well will trap electrons along the width and the depth of the device and therefore, allow transport only along the length of the device (z-axis). Since the energy levels are quantized laterally, the distribution of electrons as well as available energy states is also altered. To enable an in depth understanding of distribution and transport phenomena in these 2D wells, the 1D density of states function needs to be defined. This along with the distribution function will determine the occupancy of the states, which would lead to determination of electron line density in the nanowire.

The density of states is defined as the number of states per unit energy per unit volume of *real* space [13]. Namely,

$$\rho(E) = \frac{dN}{dE}$$

where 'N' is the number of states per unit volume of free space.

From the solution of the Schrödinger's equation for the free-electron problem, in the periodic boundary condition case, k-values are restricted to value,

$$k_x = \frac{2\pi n_x}{L}; k_y = \frac{2\pi n_y}{L}; k_z = \frac{2\pi n_z}{L}$$

where k_x, k_y, k_z are the in-plane quasi-momentum vectors in x, y and z directions and are n_x, n_y, n_zpositive and negative integers. For the 1D case, electrons are restricted to x axis and hence N will be restricted to a region along a line as shown in figure 1.6 [13] .

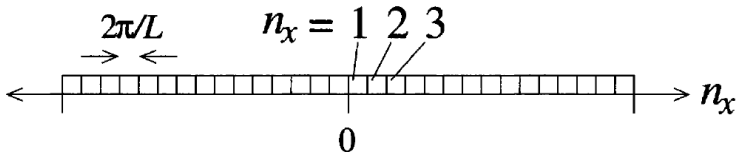

Figure 1.6 The 1-dimensional line density. The available states are restricted to this line.

The final expression for 1D density of states function is given as

$$\rho^{1D} = \frac{1}{\pi}\left(\frac{m^*}{2\hbar}\right)^2 \frac{1}{\sqrt{E}} \tag{1.7}$$

If there are n number of confined states within the quantum well system, then the density of states $\rho^{1D}(E)$ at any specific energy level is the sum total of all the subbands below that energy level, which can be represented as

$$\rho^{1D} = \sum \frac{1}{\pi}\left(\frac{m^*}{2\hbar}\right)^2 \frac{1}{sqrt(E - Ei)}\theta(E - Ei) \tag{1.8}$$

where Ei is the current Subband energy level and θ is a Heaviside step function.

1.5 Organization of the Thesis

This thesis is organized as follows: A Schrödinger-Poisson solver is developed for the above described structure and described in Chapter 2. Then, in Chapter 3, scattering mechanisms and overlap integrals used in the Monte Carlo Solver, are discussed. Development of a one-dimensional Monte Carlo solver is discussed in Chapter 4 and simulation results are presented in Chapter 5.

CHAPTER 2

SCHRÖDINGER - POISSON SOLVER

Poisson's Equation describes the relationship between the charges present in the system and the electrostatic potential. It arises out of Gauss's law for electrostatics and relates the charge density to the Laplacian of the electrostatic potential

$$\nabla.(\varepsilon\nabla\varphi) = -\rho \tag{2.1}$$

where ρ is the charge density and ε is the dielectric permittivity.

The solver developed as part of this work does a self-consistent solution of Poisson's equation and Schrödinger's equation and determines the potential profile, conduction band profile, the subband energies as well as the line density of electrons in the nanowire. The solver first proceeds to determine a semiclassical solution, that is, the quantum confinement is not being considered in the initialization stage. Poisson's equation is solved iteratively until a desired tolerance is reached. The resulting conduction band profile is stored for use in the Schrödinger solver.

The Schrödinger solver works on a much finer mesh in a smaller subset of the whole device, namely the nanowire region. The conduction band profile provides the confining potential for the 2D Schrödinger equation. The Eigenvalues and Eigenvectors determined by the solution of the Schrödinger equation are the subband energies of the 2D well and wavefunctions of the confined electrons respectively. The resulting electron density is fed back to the Poisson solver to calculate the updated potential. This procedure is repeated until a desired tolerance is reached to arrive at the self-consistent solution of the Schrödinger-Poisson equation. Subsequent sections will describe in the detail the discretization procedures as well as the solution method in detail.

2.1 Linearization and Discretization of the 2-dimensional Poisson's Equation

The 2 dimensional Poisson's Equation is given as

$$\frac{\partial}{\partial x \partial y}\left(\varepsilon(x,y)\frac{\partial}{\partial x \partial y}\varphi(x,y)\right) = -\rho(x,y) \tag{2.2}$$

Where $\varepsilon(x,y)$ is the spatially varying dielectric permittivity, $\varphi(x,y)$ is the potential and $\rho(x,y)$ is the charge density.

To solve this equation numerically, a discretization scheme such as a finite element scheme or a finite difference scheme is routinely employed [14]. This work uses finite difference discretization in the Schrödinger-Poisson solver.

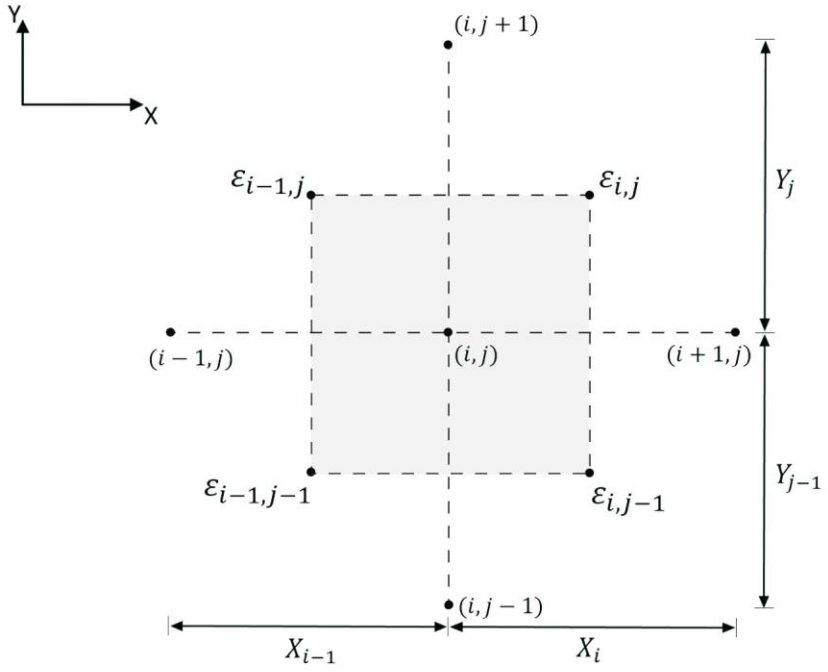

Figure 2.1 Five-point stencil used in 2-dimensional discretization of Poisson's equation

Consider the five-point stencil as shown in figure 2.1. X_i and Y_j indicate the grid sizes at the i^{th} and j^{th} node points along the x and y direction respectively. The outer differential in the Poisson's equation is determined at the midpoints of the grid. If the values of the

permittivity are known in the four quadrants, the value of ε at the midpoints is then simply a weighted average of the permittivity at the neighboring node points.

Numerically,

$$\frac{\partial}{\partial x \partial y}\left(\varepsilon(x,y)\frac{\partial}{\partial x \partial y}\varphi(x,y)\right) = \frac{\varepsilon\frac{\partial \varphi}{\partial x}_{|(i+\frac{1}{2},j)} - \varepsilon\frac{\partial \varphi}{\partial x}_{|(i-\frac{1}{2},j)}}{0.5(X_i + X_{i-1})} + \frac{\varepsilon\frac{\partial \varphi}{\partial y}_{|(i,j+1/2)} - \varepsilon\frac{\partial \varphi}{\partial y}_{|(i,j-1/2)}}{0.5\left(Y_j + Y_{j-1}\right)} \tag{2.3}$$

Where the subscripts in the numerator indicate the grid mid-points.

Expanding the inner differential as

$$\frac{\partial \varphi}{\partial x}_{|(i+\frac{1}{2},j)} = \frac{\varphi(i+1,j) - \varphi(i,j)}{Xi} \tag{2.4}$$

Using the inner stencil to compute the value of ε at the midpoints,

$$\varepsilon_{i,j+\frac{1}{2}} = \frac{\varepsilon(i,j) + \varepsilon(i,j-1)}{2} \tag{2.5}$$

Computing the values of the differentials at other node midpoints similar to Equation 2.4 and 2.5 and back substituting into Equation 2.3, one arrives at the discretized form of the left-hand side of the Poisson's equation.

$$\begin{aligned}\big(\varepsilon(i,j) + \varepsilon(i,j-1)\big)\frac{\varphi(i+1,j) - \varphi(i,j)}{(X_i(X_i + X_{i-1}))} + \big(\varepsilon(i,j) + \varepsilon(i-1,j)\big)\frac{\varphi(i,j+1) - \varphi(i,j)}{(Y_j(Y_j + Y_{j-1}))} \\ + \big(\varepsilon(i-1,j) + \varepsilon(i-1,j-1)\big)\frac{\varphi(i-1,j) - \varphi(i,j)}{(X_{i-1}(X_i + X_{i-1}))} \\ + \big(\varepsilon(i-1,j-1) + \varepsilon(i,j-1)\big)\frac{\varphi(i,j-1) - \varphi(i,j)}{(Y_{j-1}(Y_j + Y_{j-1}))} = \rho_{ij}\end{aligned} \tag{2.6}$$

Rearranging the above equation in the form of coefficients and introducing a forcing function in the right-hand side of the equation;

$$A_{ij}\,\varphi_{i,j-1} + B_{ij}\,\varphi_{i-1,j} + C_{ij}\,\varphi_{i,j} + D_{ij}\,\varphi_{i+1,j} + E_{ij}\,\varphi_{i,j+1} = \ f_{i,j} \tag{2.7}$$

The coefficients can then be expressed as

$$A_{ij} = \frac{\varepsilon(i-1,j-1) + \varepsilon(i,j-1)}{(Y_{j-1}(Y_j + Y_{j-1}))} \tag{2.8}$$

$$B_{ij} = \frac{\varepsilon(i-1,j) + \varepsilon(i-1,j-1)}{(X_{i-1}(X_i + X_{i-1}))} \tag{2.9}$$

$$D_{ij} = \frac{\varepsilon(i,j) + \varepsilon(i,j-1)}{(X_i(X_i + X_{i-1}))} \tag{2.10}$$

$$E_{ij} = \frac{\varepsilon(i,j) + \varepsilon(i-1,j)}{(Y_j(Y_j + Y_{j-1}))} \tag{2.11}$$

$$C_{ij} = -\left(A_{ij} + B_{ij} + D_{ij} + E_{ij}\right) \tag{2.12}$$

2.2 Linearization of the Forcing Function

The right side of the Poisson's Equation is the charge density ρ of the system. The charge density ρ is the total density of all the charged species in the system. In order to solve the Poisson's equation, the charge density needs to be expressed as a function of φ and be linearized. The procedure is outlined below.

As seen in the discretization above, the forcing function $f_{i,j}$ is given as

$$f_{i,j} = \rho_{ij}$$

Therefore, the forcing function can be further expressed as

$$f_{i,j} = -e(p - n - N_A + N_D) \tag{2.11}$$

where e is the fundamental charge, $N_d - N_a$ is the doping concentration, p and n are electron and hole charge densities respectively.

In the semiclassical approximation, the electron and hole densities can be expressed as

$$n = n_i \exp(\frac{\varphi}{V_T})$$

$$p = n_i \exp(-\frac{\varphi}{V_T})$$

Here n_i is the intrinsic carrier concentration, φ is the potential and V_T is the thermal energy. Assuming $\varphi => \varphi + \delta$, applying $e^{\pm\delta x} = (1 \pm \delta)$ and substituting $N_d - N_a / n_i$= C; the forcing function can be expressed as[14]

$$f_{i,j} = -e(p - n + C) + \frac{e}{V_T}(p + n)\delta \tag{2.12}$$

Substituting $\delta = \varphi_{new} - \varphi_{old}$ and rearranging φ_{new} terms with left hand side of the equation, the central coefficient and the forcing function can now be written as

$$C_{ij} = -(A_{ij} + B_{ij} + D_{ij} + E_{ij}) - \frac{e}{V_T}(p + n) \tag{2.13}$$

$$f_{i,j} = -e(p - n + C) - \frac{e}{V_T}(p + n)\varphi_{old} \tag{2.14}$$

Normalizing φ with V_T, the grid sizes with Debye length (L_D) and the doping densities with the intrinsic carrier concentration (n_i), the prefactor of $\frac{e}{V_T}$ drops out. The final expression after linearization and discretization of the 2D Poisson equation is given as:

$$C_{ij} = -(A_{ij} + B_{ij} + D_{ij} + E_{ij}) - (p + n) \tag{2.15}$$

$$f_{i,j} = (p - n + C) - (p + n)\varphi_{old} \tag{2.16}$$

Equations 2.15 and 2.16 are the governing equations for the Poisson solver. The above set of equations is solved iteratively to arrive at the potential.

This work uses Successive Over relaxation method to iteratively solve the problem. Successive over relaxation is a variant of Gauss Seidel method which results in a faster

convergence [15]. SOR method employs residuals to arrive at a faster convergence. The procedure is briefly outlined below.

2.3 The Successive Over Relaxation method

For any equation $Ax = f$, If v0, v1,…vn define the approximations that converge to x. If Vi approximates x after the i[th] iteration, then the residual is defined as[16]

$$r^i = f - Av^i$$

$$v^{i+1} = v^i + \omega r^i \tag{2.17}$$

The above equation is the governing equation for SOR method, which determines the value at the next iteration. ω is the relaxation parameter which should be chosen to maximize the rate convergence. The value of ω depends on geometry, grid spacing and boundary conditions. SOR method is employed in the solution of the Poisson's equation to iteratively solve for the potential φ.

2.4 Discretization of 2D Schrödinger Equation -Varying Effective mass

It is necessary to solve for the energy states and electron wave functions in the confined 2-Dimensional well region which constitutes the nanowire. As such, it is necessary to solve Schrödinger's equation in the nanowire domain. The 2 dimensional Schrödinger's Equation is given as

$$\frac{-\hbar^2}{2}\nabla.\left(\frac{1}{m^*}\nabla\psi\right) + V(x,y)\psi(x,y) = \in \psi(x,y) \tag{2.18}$$

Here $\psi(x,y)$ is the electron wavefunction, $\in$ is the sub-band energy of the electron and $V(x,y)$ is the confinement potential.

Since the effective mass is a property of a bulk, it is not well defined near a sharp material transition. In the hypothesis of slow material composition variations in space, one can adopt

the Schrödinger equation with a spatially varying effective mass, taken to be the mass of a bulk with the local material properties [17] [18]. As given in the above equation, the effective mass is taken inside the differential operator for the case of abrupt heterojunctions.

A similar discretization technique like the one used for Poisson's equation is used for discretization of the time independent Schrödinger equation. The stencil used for discretization is shown in Figure 2.2. The outer derivative for the effective mass is determined at the midpoints of the grid along X and Y axes.

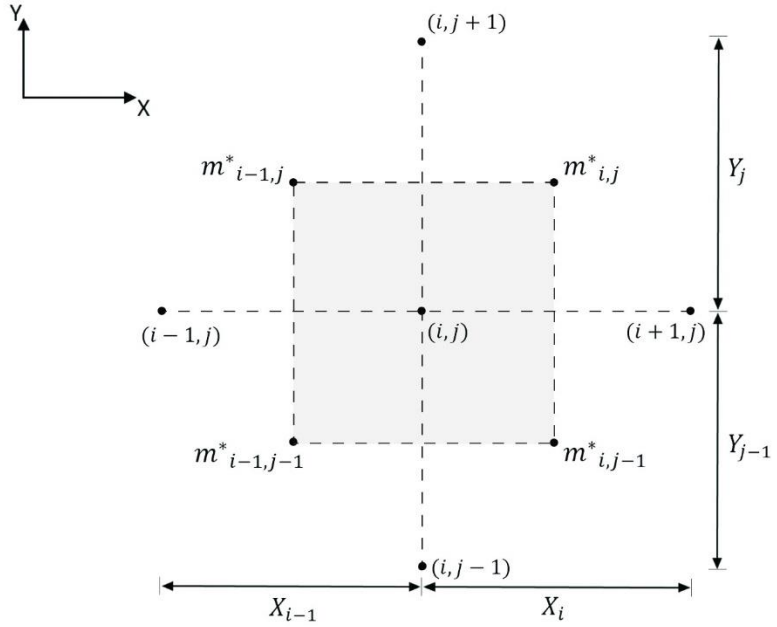

Figure 2.2 Five Point Stencil used in 2-dimensional discretization of Schrödinger's equation

The outer derivative is evaluated at point (i, j) with centered finite differences, using quantities defined at points $(i - 1/2, j)$, $(i + 1/2, j)$ and $(i, j + 1/2), (i, j - 1/2)$ respectively. Effective mass may be known only at the midpoints [18]. The abrupt

heterojunction located at point (i,j) leads to an abrupt change in effective mass at the junction. The midpoint method describes above treats this abrupt heterojunction without ambiguity. Adopting the discretization technique outlined in section 2.1 and rearranging the equation, one arrives at the following discretization coefficients for the 2 dimensional Schrödinger's equation.

$$A_{ij} = \frac{4}{m^*(i,j-1) + m^*(i-1,j-1)(Y_{j-1}(Y_j + Y_{j-1}))} \tag{2.19}$$

$$B_{ij} = \frac{4}{m^*(i-1,j) + m^*(i-1,j-1)(X_{i-1}(X_i + X_{i-1}))} \tag{2.20}$$

$$D_{ij} = \frac{4}{m^*(i,j) + m^*(i,j-1)(X_i(X_i + X_{i-1}))} \tag{2.21}$$

$$E_{ij} = \frac{4}{m^*(i-1,j) + m^*(i,j)(Y_j(Y_j + Y_{j-1}))} \tag{2.22}$$

$$C_{ij} = -\left(A_{ij} + B_{ij} + D_{ij} + E_{ij}\right) + V_{ij} \tag{2.23}$$

Here m^* is the effective mass at the given node points and V_{ij} is the confining potential which is given by the conduction band profile determined by the solution of the Poisson Solver.

The discretization coefficients are formed into a matrix $\hat{H}$ (Hamiltonian Matrix) and written in the form of an eigenvalue equation.

$$\hat{H}\psi = \in \psi \tag{2.24}$$

This is a real non-symmetric eigenvalue problem which can be solved using subroutines found in the LAPACK module [19]. This work makes use of the "sgeevx" subroutine provided by the LAPACK module for FORTRAN90. The subroutine solves a real general matrix and determines the eigenvalues and the left (or right) eigenvectors. The eigenvalues and eigenvectors so found form the subband energies and the wavefunctions.

2.5 Subband Density and Quantum Electron Density

The required number of eigenvalues and the corresponding eigenvectors are determined by solving the eigenvalue equation stated previously. The subband occupation (or line density) is determined by the product of 1D density of states function with the Fermi Dirac distribution function.

$$N_l = \int_{E_i}^{\infty} f(E)g(E)dE \tag{2.25}$$

Here N_l is the line density of subband E_i and $f(E)$ and $g(E)$ are the distribution function and the density of states function respectively.

$$f(E) = \frac{1}{1 + \exp\left(\frac{E - E_F}{\kappa T}\right)} \tag{2.26}$$

$$g(E) = \frac{\sqrt{2m^*}}{\pi\hbar}\frac{1}{\sqrt{E - E_i}}\theta(E - E_i) \tag{2.27}$$

Here, $\theta(E - E_i)$ is a Heaviside step function allowing states only above the given Subband energy E_i. Upon solving, we arrive at the following expression for the line density for given Subband E_i in the nanowire.

$$N_l^i = \frac{\sqrt{2m^*\kappa T}}{\pi\hbar} F_{-\frac{1}{2}}(\eta_i) \tag{2.28}$$

$$\eta_i = \frac{E_F - E_i}{\kappa T}$$

$F_{-\frac{1}{2}}$ is the Fermi integral which can be evaluated by standard analytical expressions [17][20]. The electron wavefunctions are obtained by normalizing the Eigen vectors and using the fact that

$$\iint_{-\infty}^{\infty} \|\psi(x,y\|^2 \, dx \, dy = 1 \tag{2.29}$$

The above equation (2.29) is integrated over the nanowire mesh. The resulting factor is used to normalize the eigenvectors to yield the wavefunctions.

The electron density in the nanowire (the Volume density) is then determined by multiplying the line density with the magnitude squared of the electron wave function and then summing it over all subbands 'm'. Numerically

$$n(x,y) = \sum_{i=1}^{m} N_l^i |\psi(x,y)|^2 \tag{2.30}$$

here $n(x,y)$ is the electron density in the nanowire calculated quantum mechanically considering the quasi 1D nature of the region. The Hartree potential, the subband energies and the electron density are all calculated self consistently as outlined below in figure 2.3.

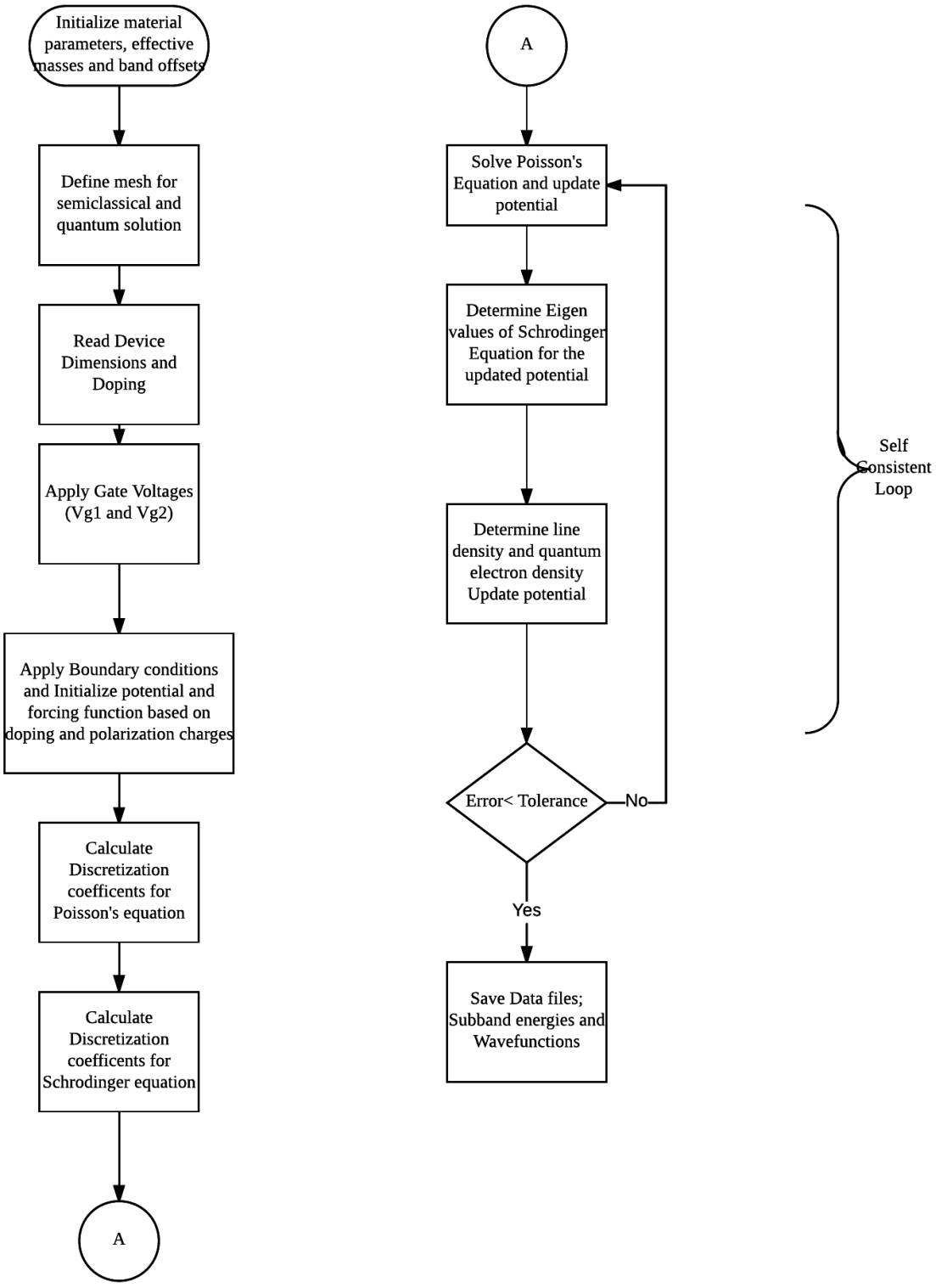

Figure 2.3 Flowchart for the self-consistent solution of the Schrödinger-Poisson solver.

2.6 Initialization and self-consistent solution

The entire self-consistent loop is depicted in the flowchart shown in Figure 2.3. Some of the steps involved are also discussed in detail below.

1. *Initialization:*

The material parameters for the heterostructure is calculated. The polarization parameters are also calculated. After the device structure is read from file, the domains are set and doping is defined. Non-uniform mesh is set accordingly in semiclassical and quantum mechanical (nanowire) domains. The polarization charges so calculated are added to the interfaces. The potential φ is then initialized per the charge neutrality conditions assuming complete ionization of dopant atoms. Since this is a heterostructure, the band parameters (Vn and Vp) are also added to the overall potential φ for calculating the carrier densities. Vn and Vp are Heterostructure band parameters which arise due to the conduction band offsets at the heterojunction [21]. The band parameters are given by

$$Vn = \chi - \chi_{ref} - \left(Eg - Eg_{ref}\right) + \left(\frac{\kappa T}{q}\log\frac{Nc}{Nc_{ref}}\right) \tag{2.31}$$

$$Vp = \chi - \chi_{ref} - \left(Eg - Eg_{ref}\right) + \left(\frac{\kappa T}{q}\log\frac{Nv}{Nv_{ref}}\right) \tag{2.32}$$

Here χ, $\chi_{ref,}$ Eg and Eg_{ref} are the electron affinities and band gaps at a given node point and at a reference point respectively. Nc, Nv and Nc_{ref}, Nv_{ref} are the effective density of states of the conduction band and valence band at the given node point and at a reference point respectively.

2. *Boundary Conditions:*

Dirichlet boundary conditions exist at the dual gates, while the other boundaries of the device are under Neumann boundary conditions.

3. *Output Files:*

Once the solution converges, the potential profile, the subband density, the electron density and the wavefunctions for all the subbands are exported to the Monte Carlo solver.

The following chapter will introduce scattering rates which will be a prerequisite for the 1 dimensional Monte Carlo solver development.

CHAPTER 3

PHONON SCATTERING MECHANISMS

Understanding the dominant scattering processes in the material is a crucial step in determining the low-field mobility. Although scattering is detrimental to the device, it is what dictates the transport in the device.

This chapter discusses the scattering mechanisms relevant for studying transport in the nanowire. The Bandstructure considered for gallium nitride is a single valley (Γ_1) non-parabolic band model with non-parabolicity ($\alpha = 0.189$ eV^{-1}). The scattering mechanisms considered are electron-phonon interactions such as acoustic phonon scattering, polar optical phonon scattering and piezoelectric scattering.

The scattering processes which interrupt the carrier free-flights are calculated quantum mechanically. The scattering event is treated by defining a scattering potential, which is calculated for each type of scattering process. Each of the different processes, or interactions leads to a different "matrix element" form in terms of its dependence on the initial wave vector, the final wave vector and their corresponding energies.

Scattering processes for Quasi 1D systems differ from their bulk counterparts as confined scattering rates also involve overlap integrals arising from the electron wavefunctions overlaps of different states [22].

The electron wavefunctions are plane waves in the unconfined z-axis and obtained from the Schrodinger Poisson Solver in the confined x-y plane. Therefore, the electron wavefunctions for the initial and final states are given by

$$\Psi_n(kz) = \frac{1}{\sqrt{L}}\psi_n(x,y)\exp(\mathrm{kz.\,z}) \tag{3.1}$$

$$\Psi_m(kz') = \frac{1}{\sqrt{L}}\psi_m(x,y)\exp(\mathrm{kz'.\,z}) \tag{3.2}$$

Here L is the length of the quasi 1D region, ψ (x, y) is obtained by solving the Schrödinger's equation and z is the position vector along the unconfined direction. Overlap integrals play a crucial role in confined scattering processes as they dictate the matrix element and hence the scattering rates out of state kz and subband n.

As the carriers are confined in the two-dimensional quantum well, the uncertainty in the momentum increases which follows directly as a result of uncertainty principle.

$$\Delta kx.\,\Delta x \geq \frac{\hbar}{2} \tag{3.3}$$

$$\Delta ky.\,\Delta y \geq \frac{\hbar}{2} \tag{3.4}$$

Since the wavefunctions of electrons are known in the confined directions, the uncertainty in the momentum becomes infinite [22]. This directly results in momentum conservation being valid only in the unconfined z plane since there is well defined momentum only in this plane.

The matrix element for any scattering process is given by

$$M(kz, kz') = \frac{1}{L}\int \exp(i(kz - kz').z)\,dz \iint \psi_n{}^*(x,y)\hat{H}(x,y)\psi_m(x,y)dxdy \tag{3.5}$$

Here $H(x,y)$ is the perturbation potential.

Fermi's golden rule describes scattering rates from states kz in n^{th} subband to state kz' in the m^{th} subband [23].

$$Snm(kz, kz') = \frac{2\pi}{\hbar}|M(kz, kz')|^2\delta(E - E' \pm \hbar\omega) \tag{3.6}$$

Equation (3.6) is called Fermi's Golden Rule, where kz and kz' are the initial and final states of the carrier, E_k and $E_{k'}$ are the corresponding kinetic energies and $\hbar\omega_q$ is the phonon energy and $\delta(E_k - E_{k'} \pm \hbar\omega_q)$ describes the conservation of energy during the scattering process. The conservation of energy is only valid in the long-time limit, that is when the scattering events are infrequent. The top sign is for absorption and the bottom sign is for the phonon emission process.

3.1 Acoustic Phonon Scattering

Phonon scattering is due to the vibrations of the crystal lattice. Acoustic phonons are caused by the lattice atoms oscillating in the same direction. Hence acoustic phonons cause the deformation of the unit cell. This differential displacement along with the deformation potential forms the perturbation potential for acoustic phonon scattering [24]. At room temperature, Acoustic phonons have energies much less than the thermal energy, hence the interaction of electrons with them is treated as an elastic scattering. Acoustic phonons can cause either *intersubband* or *intrasubband* scattering.

The scattering potential due to acoustic phonon scattering is of the following form.

$$\widehat{H} = \Xi_{ac}\,\nabla.\boldsymbol{u}(\boldsymbol{r}) \tag{3.7}$$

Where Ξ_{ac} is the acoustic deformation potential and u(r) is the phonon unit vector given by [24]

$$u(r) = \sum_q \sqrt{\frac{\hbar}{2\rho\omega_q\Omega}}\,\boldsymbol{e_q}\left(a_q\boldsymbol{e^{iq.r}} + {a_q}^+\boldsymbol{e^{-iq.r}}\right) \tag{3.8}$$

Here $a_q, {a_q}^+$ are the creation and annihilation operators, q is the phonon wave vector, ρ is the material density, $\boldsymbol{e_q}$ is the unit polarization vector and $\hbar\omega_q$ is the phonon energy. The perturbation potential can then be found by substituting (3.8) into (3.7) [23].

$$\widehat{H}(r) = \Xi_{ac} \sum_q \sqrt{\frac{\hbar}{2\rho\omega_q\Omega}}\, \boldsymbol{q} \,.\, \boldsymbol{e_q}\left(a_q \boldsymbol{e^{iq.r}} - {a_q}^+ \boldsymbol{e^{-iq.r}}\right) \tag{3.9}$$

To arrive at the expression for the matrix element, equation (3.9) is integrated over phonon coordinates and substituted into equation (3.5) [25].

$$M_{nm}(kz, kz') = \sqrt{\frac{\hbar}{2\rho\omega_q\Omega}}\, \Xi\, \mathrm{q} \sqrt{\left(N_q + \frac{1}{2} \pm \frac{1}{2}\right)\frac{1}{L}} \ldots$$

$$\int \exp(i(kz - kz' \pm qz))\, dz \iint \psi_n(x,y) \exp\left(i\left(q_x x + q_y y\right)\right) \psi_m(x,y) dx dy \tag{3.10}$$

Here N_q is the phonon number density given by the Bose-Einstein distribution function

$$N_q = \frac{1}{\mathrm{e}^{\frac{\hbar\omega_q}{\kappa T}} - 1} \tag{3.11}$$

Under the elastic and equipartition approximation [24], one can assume that the phonon energy is much less than thermal energy ($\hbar\omega_q \ll \kappa T$). Thus, in addition to the interactions with electrons being elastic, it also leads to

$$N_q = N_q + 1 \cong \frac{\kappa T}{\hbar\omega_q} \tag{3.12}$$

For low energies, the dispersion curve for acoustic phonons is linear, therefore one can approximate

$$\omega_q = v_s q \tag{3.13}$$

Here v_s is the sound velocity in the material.

Furthermore,

$$\frac{1}{L}\int \exp\big(i(kz - kz' \pm qz)\big)\, dz = \delta(kz - kz' \pm qz) \tag{3.14}$$

$$\iint \psi_m(x,y) \exp\Big(i\big(q_x x + q_y y\big)\Big) \psi_n(x,y) dxdy = \; {I_{nm}}^{ac}(qx, qy) \tag{3.15}$$

The overlap integral for acoustic scattering is denoted by ${I_{nm}}^{ac}(qx, qy)$. From Equations (3.11) to (3.15), the matrix element can then be written as

$$|M(kz, kz')|^2 = \frac{\Xi^2 \kappa T}{2\rho\Omega v_s^2} |{I_{nm}}^{ac}(qx, qy)|^2 \delta(kz - kz' \pm qz) \tag{3.16}$$

Substituting (3.16) into equation (3.6) and integrating over all final states kz', one arrives at the final expression for Acoustic Scattering rate from subband m to subband n.

$$\Gamma_{nm}^{ac} = 2 \sum_{kz'q} Snm(kz, kz') \tag{3.17}$$

Where the prefactor of 2 accounts for absorption and emission of phonons. Substituting the expression for $Snm(Kz, Kz')$ from Fermi's golden rule and converting the summation to an integral, equation (3.17) expands to

$$\Gamma_{nm}^{ac} = 2\frac{2\pi}{\hbar}\frac{\Xi^2 \kappa T}{2\rho\Omega v_s^2}\frac{1}{2\pi}$$

$$\iint \frac{1}{(2\pi)^2} |{I_{nm}}^{ac}(qx, qy)|^2 dq_x dq_y \int \delta(kz - kz' \pm qz)\, \delta(E - E') dkz' \tag{3.18}$$

Converting the integration variable in the delta function integral from dkz' to dE' where E' is the final energy after scattering, the delta function integral evaluates to the final density of states function [25]

$$\int \delta(kz - kz' \pm qz)\, \delta(E - E')dkz' = \sqrt{\left(\frac{2m}{\hbar^2}\right)} \frac{\left(1 + 2\alpha E_f\right)}{\sqrt{E_f\left(1 + \alpha E_f\right)}} \tag{3.19}$$

Where $E_f = E_n - E_m + E_i$, is the final energy after scattering, E_n and E_m are subband energies and E_i is the initial electron energy.

Evaluating the integral of overlap function $|{I_{nm}}^{ac}(qx, qy)|^2$ one arrives at the following expression [26]

$$I_{overlap}^{acoustic} = \iint \frac{1}{(2\pi)^2} |{I_{nm}}^{ac}(qx, qy)|^2 dq_x dq_y = \iint |\psi_m(x, y)|^2 |\psi_n(x, y)|^2 dxdy \tag{3.20}$$

The overlap integral is evaluated over the entire quasi 1D region. Substituting (3.20) and (3.19) into (3.18), the final scattering rate for Acoustic Phonons is given by

$$\Gamma_{nm}^{ac} = \frac{\Xi^2 \kappa T \sqrt{2m^*}}{2\rho v_s^2 \hbar^2} I_{overlap}^{acoustic} \frac{\left(1 + 2\alpha E_f\right)}{\sqrt{E_f\left(1 + \alpha E_f\right)}} \Theta\left(E_f\right) \tag{3.21}$$

Here the step function $\Theta\left(E_f\right)$ allows only those transitions when the final energy is positive.

Acoustic scattering rate decreases with increasing energy. Hence acoustic phonons are primarily active at low electron energies.

3.2 Polar Optical Phonon Scattering

Polar Scattering occurs in materials having two different kinds of atoms in their basis. In such crystals, there is charge transfer in between the two atoms creating a dipole moment. Polar Scattering can be due to optical phonons (polar optical phonon scattering) and acoustic phonons (piezoelectric scattering). This section discusses the scattering due to

Optical phonons. Since GaN is a highly polar material, Polar optical phonon scattering would be a dominating factor in determining the mobility of the GaN nanowire.

Optical phonons arise out of lattice vibrations wherein the constituent atoms oscillate in opposite directions creating a relative displacement. This does not induce lattice strain, rather alters the size of unit cell [24]. Therefore, any perturbation potential arising out of optical phonon interaction is a product of the optical deformation potential and the lattice displacement.

$$\hat{H} = \mathrm{D}_o \boldsymbol{u}(\boldsymbol{r}) \tag{3.22}$$

In polar materials, the optical phonons cause oscillatory behavior in the existing dipole. Electrons are scattered by this long-range dipole field which oscillates in time and space [27]. This forms the basis of the perturbing potential. Although there is no clear distinction between Longitudinal mode(LO) and Transverse Mode (TO) optical phonons in Wurtzite materials [25], it is seen that LO phonons have higher scattering rates than TO phonons [28]. A detailed discussion on LO and TO phonons in wurtzite materials would be beyond the scope of this thesis. This work would consider only the longitudinal Mode(LO) optical phonons as participating in polar optical scattering. The interaction between LO optical phonons and electrons is called Froehlich interaction and the so derived Froehlich Hamiltonian is used in determination of the matrix element.

The polarization field arising out of displacement of atoms in the unit cell due to the propagation of optical phonon is given by [29]

$$\boldsymbol{P}(r) = \frac{e^*}{\Omega}\boldsymbol{u}(r) \tag{3.23}$$

Here **u**(r) is the lattice displacement vector, e* is the effective charge and Ω is the unit cell volume. The effective charge is further given by[29]

$$e^{*^2} = \mu\Omega\omega_{LO}^2\left(\frac{1}{\varepsilon_\infty} - \frac{1}{\varepsilon(0)}\right) \tag{3.24}$$

Here μ is the relative mass of the atoms in the unit cell, ω_{LO} is the LO optical phonon frequency. ε_∞ and $\varepsilon(0)$ are the high frequency and static dielectric constants respectively. Using equation (3.8) for the phonon displacement vector and the using the fact that in the absence of free charge the divergence of displacement field is zero, that is

$$\nabla.\boldsymbol{D} = 0$$

$$q(\varepsilon\boldsymbol{E} + \boldsymbol{P}) = 0 \tag{3.25}$$

Where **E** is the induced electric field.

From the above equations (3.23) -(3.25), the Froehlich Hamiltonian [29]can be derived as

$$\widehat{H}_{pop} = \frac{iee^*}{\varepsilon_\infty\Omega}\sum_q \sqrt{\frac{\hbar}{2\mu N\omega_q}}\frac{1}{q}\left(a_q\boldsymbol{e^{iq.r}} - a_q{}^+\boldsymbol{e^{-iq.r}}\right) \tag{3.26}$$

Following the approach taken in acoustic phonon scattering, the matrix element is determined by integrating the above equation over phonon coordinates.

$$M(kz, kz') = \frac{iee^*}{\varepsilon_\infty\Omega}\sqrt{\frac{\hbar}{2\mu N\omega_q}}\frac{1}{q}\sqrt{\left(N_q + \frac{1}{2} \pm \frac{1}{2}\right)}\frac{1}{L} \ldots$$

$$\int \exp\left(i(kz - kz' \mp qz)\right)dz \iint \psi_n(x,y)\exp\left(i\left(q_x x + q_y y\right)\right)\psi_m(x,y)dxdy \tag{3.27}$$

Using equation (3.24) for e* and using the fact that $\omega_q = \omega_{LO}$ for optical phonons, one can obtain,

$$|M(kz,kz')|^2 = \frac{\hbar e^2 \omega_{LO}}{2V}\left(\frac{1}{\varepsilon_\infty}-\frac{1}{\varepsilon(0)}\right)\frac{1}{q^2}\left(N_q+\frac{1}{2}\pm\frac{1}{2}\right)\ldots$$

$$|{I_{nm}}^{pop}(qx,qy)|^2\delta(kz-kz'\mp qz) \tag{3.28}$$

Where the double integral over the wavefunctions has been re-written as ${I_{nm}}^{pop}(qx,qy)$

$$\iint \psi_m(x,y)\exp\left(i\left(q_x x+q_y y\right)\right)\psi_n(x,y)dxdy = {I_{nm}}^{pop}(qx,qy)$$

and $N_q+\frac{1}{2}\pm\frac{1}{2}$ takes into account the absorption and emission of phonons respectively.

Using Fermi's golden rule for determining the scattering rate $Snm(Kz,Kz')$ and summing up over all final states Kz', the final polar optical phonon scattering rate from subband m to subband n is given as[25]

$$\Gamma_{nm}^{pop} = \frac{e^2\omega_{LO}}{8\pi^2}\left(\frac{1}{\varepsilon_\infty}-\frac{1}{\varepsilon(0)}\right)\left(N_q+\frac{1}{2}\pm\frac{1}{2}\right)\iint\frac{1}{q^2}|{I_{nm}}^{pop}(qx,qy)|^2 dq_x\, dq_y$$

$$\int dkz'\,\delta(kz-kz'\mp qz)\,\delta(E-E'\pm\hbar\omega_0) \tag{3.29}$$

The delta function integral is calculated similar to the approach adopted for Acoustic Scattering by converting dkz' to dE'[25],

$$\int \delta(kz-kz'\mp qz)\,\delta(E-E')dkz' = \sqrt{\left(\frac{2m}{\hbar^2}\right)}\frac{\left(1+2\alpha E_f\right)}{\sqrt{E_f\left(1+\alpha E_f\right)}}$$

Here E_f now considers absorption or emission of Optical phonon as well, that is

$$E_f = E_n - E_m + E_i \pm \hbar\omega_{LO} \tag{3.30}$$

The calculation of the overlap integral ${I_{nm}}^{pop}(qx,qy)$ is discussed below.

3.2.1 Evaluation of the Overlap Integral: Forward and Backward Scattering

The rate of polar optical phonon scattering in confined systems such as the nanowire in this case depends on the overlap integral which couples the initial and final electron states. The overlap integral appearing in equation (3.29) contains the wavefunctions of the initial and final state as well as the phonon wave vector **q** with components q_x, q_y and q_z**.** One can define the components along the confined directions (q_x and q_y) as

$$q_{x,y} = \frac{2\pi}{L_{x,y}} \frac{n}{100} n = 1,2,3 \ldots$$

Where 1/100 is an arbitrarily chosen prefactor.

Along the transport direction z, the phonon wave vector (q_z) takes a form depending on the initial and final electron wavevectors kz and kz'. The process is derived below.

$$\iint \frac{1}{q_x^2 + q_y^2 + q_z^2} |I_{nm}{}^{pop}(qx, qy)|^2 dq_x \, dq_y = I_{overlap}^{pop}(qz)$$

$$kz' = kz + q_z$$

$$kz'^2 = q_z^2 + 2kzq_z \cos\theta + kz^2 \tag{3.32}$$

Since the electrons travel only along positive (or negative) z axis, $cos\theta$ can take only two values ± 1. Based on the two values, the electrons can either undergo <u>forward</u> ($cos\theta = 1$) or <u>backward</u> ($cos\theta = -1$) scattering. Therefore, the phonon wave vector can take on two possible values

$$q_z = -kz + kz' \tag{3.33}$$

Which corresponds to forward scattering and

$$q_z = kz + kz' \tag{3.34}$$

Which corresponds to backward scattering. kz and kz' are electron wavevectors before and after scattering respectively.

Finally, the overlap integral for polar optical phonon scattering between electron states in subband n and subband m is calculated by determining $\left|{I_{nm}}^{pop}(q_x, q_y)\right|^2$ numerically by using equation (3.33) and (3.34) to calculate the integral in equation (3.32).

The resulting overlap factor $I_{overlap}^{pop}(q_z)$ is substituted back into Equation (3.29) to get

$$\Gamma_{nm}^{pop} = \frac{e^2\omega_{LO}}{8\pi^2}\left(\frac{1}{\varepsilon_\infty} - \frac{1}{\varepsilon(0)}\right)\sqrt{\left(\frac{2m}{\hbar^2}\right)}\left(N_q + \frac{1}{2} \pm \frac{1}{2}\right) I_{overlap}^{pop}(qz)\frac{\left(1 + 2\alpha E_f\right)}{\sqrt{E_f\left(1 + \alpha E_f\right)}} \quad (3.35)$$

Polar optical scattering is q-vector dependent and favors small angle scattering, which as seen in later chapters, in quasi 1D systems favors Forward scattering against backward scattering.

3.3 Piezoelectric Scattering

Piezoelectric scattering is a type of polar scattering which is effected by acoustic phonons. As described in section 3.2, charge transfer occurs in polar materials which creates a dipole. Second order interaction of electrons with these fields gives rise to Piezoelectric scattering which is discussed here. Piezoelectric polarization is proportional to the acoustic strain which further depends on differential displacement [24]. Numerically

$$\boldsymbol{P} = e_{pz}\nabla.\,\mathrm{u}(\mathbf{r}) \quad (3.36)$$

Where e_{pz} is a piezoelectric constant which depends on the piezoelectric and elastic properties of the material [30]. Similar to the one obtained for polar optical phonon scattering, the perturbing Hamiltonian is given by[30]

$$\widehat{H}_{piezo} = -\frac{ee_{pz}}{\varepsilon_\infty}\sum_q \sqrt{\frac{\hbar}{2\mu N\omega_q}}\left(a_q \boldsymbol{e^{iq.r}} + a_q{}^{+}\boldsymbol{e^{-iq.r}}\right) \tag{3.37}$$

Integrating over phonon coordinates along with initial and final electron states to get the Matrix Element[25]

$$M(kz,kz') = -\frac{ee_{pz}}{\varepsilon_\infty \Omega}\sqrt{\frac{\hbar}{2\mu N\omega_q}}\sqrt{\left(N_q+\frac{1}{2}\pm\frac{1}{2}\right)}\frac{1}{L}\ldots$$

$$\int \exp\left(i(kz-kz'\mp q_z)\right)dz \iint \psi_n(x,y)\exp\left(i\left(q_x x+q_y y\right)\right)\psi_m(x,y)dxdy \tag{3.38}$$

Since this scattering mechanism is acted upon by acoustic phonons, at low energies, one can use the elastic and equipartition approximation to write

$$N_q = N_q + 1 \cong \frac{\kappa T}{\hbar\omega_q}$$

Since the dispersion of acoustic phonons is linear, $\omega_q = v_s q$, equation (3.37) can be transformed to

$$|M(kz,kz')|^2 = \left(\frac{ee_{pz}}{\varepsilon_\infty}\right)^2 \frac{\kappa T}{2\rho v_s^2}\frac{1}{q^2}\left|I_{nm}{}^{piezo}(qx,qy)\right|^2 \delta(kz-kz'\mp q_z) \tag{3.39}$$

Here $I_{nm}{}^{piezo}\left(q_x,q_y\right)$ is the overlap integral containing the initial and final electron states defined similarly to overlap integral in polar optical phonon scattering[25]. The overlap integral is evaluated in the method described in section 3.2.1.

The final scattering rate out of state kz and subband m is given by using Fermi's golden rule to determine the total transitions and summing it up over all final states kz'. That is

$$\Gamma_{nm}^{piezo} = 2\sum_{qz}\frac{2\pi}{\hbar}|M(kz,kz')|^2\delta(E-E') \tag{3.40}$$

The prefactor of 2 accounts for absorption and emission of acoustic phonons. The energy conserving delta function omits the phonon energy term ($\hbar\omega$) as acoustic phonons carry negligible energy at room temperature.

Expanding the Matrix element from (3.38) and converting the delta function integral from dkz' to dE', equation (3.39) becomes

$$\Gamma_{nm}^{piezo} = \left(\frac{ee_{pz}}{\varepsilon_\infty}\right)^2\frac{\kappa T\sqrt{2m^*}}{4\pi\hbar^2\rho v_s^2}I_{overlap}^{piezo}(q_z)\frac{(1+2\alpha E_f)}{\sqrt{E_f(1+\alpha E_f)}} \tag{3.41}$$

Where $E_f = E_n - E_m + E_i$

The overlap integral here is termed $I_{overlap}^{piezo}(qz)$ and is calculated using the same algorithm as that of the polar optical phonon scattering.

$$\iint\frac{1}{q_x^2+q_y^2+q_z^2}\left|I_{nm}{}^{piezo}(qx,qy)\right|^2 dq_x\,dq_y = I_{overlap}^{piezo}(q_z)$$

Similar to polar optical phonon scattering, Piezoelectric scattering also has q dependence in the overlap integral, and favors forward over backward scattering.

CHAPTER 4

THE ONE-DIMENSIONAL MONTE CARLO SOLVER

4.1 The Boltzmann Transport Equation

The Boltzmann Transport equation is given as [24]

$$\frac{\partial f}{\partial t} + \boldsymbol{v}.\nabla_r f + \boldsymbol{F}.\nabla_p f = s(\boldsymbol{r}, \boldsymbol{p}, t) + \frac{df}{dt}|_{coll} \tag{4.1}$$

The distribution function is denoted by $f(r, k, t)$. It is a complicated integro-differential equation in seven-dimensional phase space. Three dimensions each in momentum (k) space and real space and one in time. The left-hand side of equation (4.1) consists of three terms, the first term describes the time variation of the distribution function f, the second term describes the spatial variation of the distribution function and finally the third term describes the effect on the distribution function due to applied fields [31]. On the right-hand side, the first term describes the recombination and generation processes and the second term is the collision integral which describes the scattering processes [31]. Analytical solution of the BTE requires unrealistic approximations which may not lead to desired results.

Therefore, stochastic methods such as Monte Carlo are best suited to solve the Boltzmann Transport Equation. There are three approaches to solving a BTE using Monte Carlo:

- Single Particle Monte Carlo - in which the motion of a single particle is tracked for an extended period of time until it reaches steady state.
- Ensemble Monte Carlo - A large number of particles (hence an ensemble) are simulated at the same time. This is particularly useful in transient analysis as it

allows for average quantities to be computed by 'freezing' the simulation at regular intervals dt.

- Self-consistent Monte Carlo - The ensemble Monte Carlo solver is coupled with a Poisson equation solver and self consistently solved which also tracks changes in potential with time. This approach is best suited for a full simulation of any device.

This work employs the Ensemble Monte Carlo method to calculate mobility of the nanowire along the transport (unconfined) direction.

4.2 Self-scattering and Free Flight

The free-flight scatter routine forms the basis of every Monte Carlo algorithm. Hence it is imperative to understand the underlying methodology to calculate the free flight time and scatter rates. As seen previously, the scattering rate for each scattering mechanism is a function of the electron energy and hence the total scattering rate is also a function of the energy of the particles.

Consider an electron in a system. If $\Gamma[k(t)]dt$ is the probability that an electron in state k suffers a collision during the time interval dt, then the probability that an electron which has had a collision at time t=0 has not yet undergone another collision after time t is [24],

$$P = e^{-\int_0^t \Gamma[k(t)]dt} \tag{4.2}$$

Therefore, the probability $P(t)$ that the electron will suffer a collision during dt around t is given by

$$P(t)dt = \Gamma[k(t)]e^{-\int_0^t \Gamma[k(t)]dt} \tag{4.3}$$

Random free flight times can be generated by integrating the left-hand side of (4.3) to the desired free-flight time τ_r such that

$$r = \int_0^{\tau_r} P(t)dt \tag{4.4}$$

Where r is a uniformly distributed random number between [0.1]. Substituting (4.3) in (4.4) gives

$$-\ln r = \int_0^{\tau_r} \Gamma[k(t)]dt \tag{4.5}$$

The above integral gets very complicated to solve analytically due to the presence of energy dependent total scattering rate $\Gamma(k)$. In order to simplify and make the integral trivially solvable, a scattering term called self-scattering (Γ_{ss}) is introduced [24]. Self-scattering does not change the momentum or the energy of the particle and therefore does not change the physics of the particle. The self-scattering adjusts in such a way that the total scattering rate is constant in time. Numerically,

$$\Gamma_T = \Gamma\big(k(t)\big) + \Gamma_{ss} \tag{4.6}$$

Since the self-scattering term has no effect on the physics of the particle, it, therefore, does not change the free-flight of the particle, therefore equation (4.5) is converted to

$$\tau_r = -\frac{1}{\Gamma_T}\ln r \tag{4.7}$$

From (4.7) it is evident that the total scattering rate must be determined for the range of energy values, in other words, a *scattering table* containing the scattering rates for all N scattering mechanisms should be formed. The particle is *drifted* under the applied Field E for the free-flight time so determined.

4.3 Scattering Table and Renormalization

The expression for scattering rates of different scattering mechanisms has been derived in Chapter 3. This section discusses the methodology to determine the total scattering rate and the maximum scattering rate Γ_{max}. This is followed by renormalization of the scattering table with Γ_{max}. This procedure is necessary as it allows selection of a scattering mechanism based on a uniformly distributed random number.

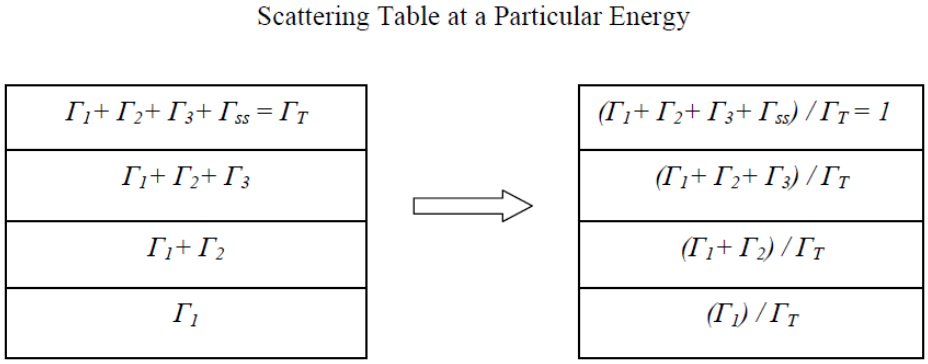

Figure 4.1 Scatter table creation and normalization procedure [31]

Figure 4.1 outlines the procedure followed in creating a scattering table for a system having 3 scattering mechanisms ($\Gamma_1, \Gamma_2, \Gamma_3$). This process is repeated for all the subbands. The scattering table is L x M x N matrix where L is the number of subbands, M is the number of scattering processes and N is the total number of energy intervals.

After the duration of free flight elapses, the energy and the subband of the particle are extracted and then the particle is scattered according to a scattering mechanism selected according to a random number between 0 and 1. The procedure is outlined below [31].

A random number (R) is chosen between 0 and 1 and if

$$\sum_{i=0}^{j} \frac{\Gamma_i}{\Gamma_T} < R \leq \sum_{i=0}^{j+1} \frac{\Gamma_i}{\Gamma_T} \text{ where } j = 0,1,2,..n \ \Gamma_{j+1} = \Gamma_{ss} \tag{4.8}$$

then scattering type *j+1* is chosen. Here, of course, $\Gamma_0 = 0$. If self-scattering is chosen, nothing is done and the loop continues to the next particle. The final state (as well as the final subband) of the particle is then arrived at by changing the electron wave vector and the final subband depending on the scattering mechanism which the particle underwent.

4.4 Carrier Drift

For the duration of free-flight, the particle is accelerated under the applied field E according to Newtonian laws of motion. The change in momentum δk and new energy of the carriers' due to this *drift* process is obtained from the equation of motion.

$$\frac{dp}{dt} = \hbar \frac{dk}{dt}$$

Therefore,

$$\delta k = \frac{-qF}{\hbar} \tau$$

$$k_{new} = k + \delta k$$

$$E = \frac{\hbar^2 {k_{new}}^2}{2m^*}$$

$$E_{np} = \frac{-1 + \sqrt{1 + 4\alpha E}}{2\alpha} \tag{4.9}$$

where, E_{np} is the final energy after drift process considering non-parabolic bands (α is the nonparabolicity factor) and τ is the free-flight time. For quasi-1d systems such as the

nanowire considered in this work, the field F is along the unconfined direction z and hence the electron wavevector k is also calculated along z direction only.

4.5 Ensemble Averages

The ensemble Monte Carlo method does not require steady-state conditions to calculate the ensemble averages. Therefore, at regular intervals of δt, the quantities of carrier velocity and energy are averaged for every subband by counting the number of particles in each subband.

To obtain the time evolution of certain physical quantities, the simulation is 'frozen' at intervals of δt. The time steps δt at which the simulation is paused and the ensemble averages are taken should not be much larger than the maximum frequency of scattering [24]. The time interval should be chosen such that it is neither too small to introduce noise in the output, nor too large to lead to information loss [31]. Therefore, there are now two time quantities in the simulation, free-flight time and sampling time.

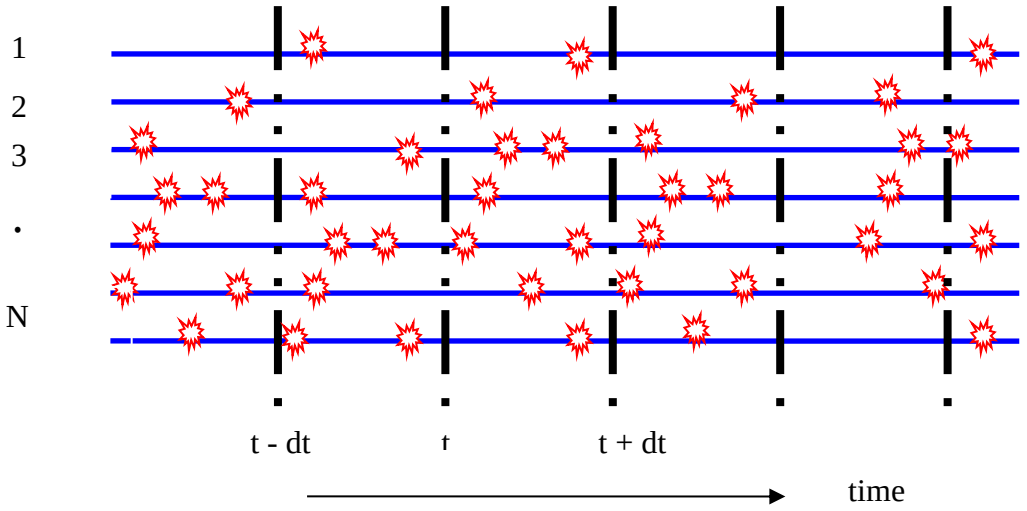

Figure 4.2 Ensemble Monte Carlo: Free flight, scatter and sampling time intervals [26]

Figure 4.2 shows the Ensemble Monte Carlo simulation in a nutshell. The number of particles (N) is represented vertically, while the time evolution of each particle proceeds horizontally along the blue line. The dashed horizontal line represents the sampling intervals of dt. Each * represents a scattering event taking place after the duration of the free-flight.

At each time interval, the ensemble averages are calculated using the following expression (for non-parabolic bands). For the nth subband, the expressions are

$$v_n(t) = \frac{1}{N_n}\sum_{i=1}^{N} v_i(t) \quad \text{and} \quad E_n(t) = \frac{1}{N_n}\sum_{i=1}^{N} E_i(t) \tag{4.10}$$

Here N_n is the number of particles in the nth subband. Further, $v_i(t)$ is calculated according to

$$v_i(t) = \frac{\hbar kz}{m^*(1+2\alpha E)} \tag{4.11}$$

Here kz is the electron wavevector along the z-direction.

4.6 The One-dimensional Monte Carlo algorithm

The previous section explained in detail the Monte Carlo procedure used in device simulations. This section provides the algorithm used in Monte Carlo Simulation of the Quasi 1D nanowire. The 1D Monte Carlo code calculates mobility by simulating transport along the unconfined *z*-direction. Electrons are moved in k space in response to field applied along the positive z-direction. This work is concerned with low field mobility; hence the applied field is restricted to a few kV/cm in the transport direction.

The entire Monte Carlo algorithm is displayed as a flowchart in figure 4.3. The code starts with the output files saved from the Schrödinger Poisson Solver. Following files are used

from the Schrodinger-Poisson Solver: a) the subband energies, b) the subband population and c) the electron wavefunctions.

As discussed in chapter 3, overlap integrals between the initial and final states are a crucial factor in the scattering rates. The number of electrons taking part in the simulation may range from 20000 to 30000. The overlap integrals for various scattering mechanisms are also calculated in this code. The major functions used in this algorithm are outlined below.

- Read_wavefunctions

This subroutine reads the files saved from the Schrodinger Poisson solver and stores them into arrays or matrices as deemed suitable. There is also a provision to change the *number of subbands* to be considered in the simulation. The *acoustic overlap integral* which is independent of energy is also calculated for the n subbands and is stored in an array.

- Scatter_table

Depending on what scattering mechanisms are enabled (determined by appropriate *flags*), the scatter table subroutine calls the appropriate subroutines to calculate the scattering rates for the scattering mechanisms as a function of energy. The scattering rates are then stored in a scatter table corresponding to the n^{th} subband (the initial subband). In addition, the final subband and the change in energy from before and after the scattering event are also stored in an array. For Polar optical phonon and piezoelectric scattering, the scattering subroutines are further divided into Absorption/emission and forward /backward scattering. The overlap integrals for Polar optical scattering and Piezoelectric scattering are dependent on energy and hence are calculated within the respective subroutines.

- Renorm_table

This subroutine normalizes the scattering rates according to the normalization procedure described previously in figure 4.1. This subroutine also calculates the *maximum gamma* for each subband which is used in calculated random free flight times for each particle depending on its subband.

- Initialization

This subroutine initializes the electrons into the subbands and assigns them a kinetic energy according to the *Boltzmann Distribution.* Since the motion of electrons is restricted to only one direction, the average energy according to a Boltzmann distribution is subsequently modified to $\frac{1}{2}\kappa T$ [24]. The momentum vector is also determined according to non-parabolic E-k relationship and assigned either a forward (+z) or a backward(-z) direction according to a uniformly distributed random variable. The electrons are distributed among different *subbands* by using the percentage population of the *subbands* obtained from the *subband density* file output by the Schrödinger-Poisson Solver [25].

- Free-Flight

Once the time loop starts this subroutine is called for every sampling time interval δt. In this routine, each particle is drifted (by calling the *drift* routine, which moves the particle under the applied field) and at the end of free flight duration, a scattering mechanism is selected according to the random variable method outlined previously. Another subroutine *scatter_angle* exists to change the electron energy, its subband, and the wavevector according to the scattering which the electron underwent. At the end of free-flight-scatter routine, the new particle attributes are mapped back to the particle array for the next time interval.

- Scatter_angle

This subroutine is called after a scattering mechanism is chosen at the end of free-flight/drift duration. The scattering mechanism is chosen as follows. After extracting the *subband* information form the electron, a *bin* is chosen to correspond to the energy of the electron. Then, the scattering mechanism is chosen according to the uniformly distributed random variable method highlighted in the previous section. The corresponding scatter angle subroutine pertinent to the scatter mechanism is then called.

The scatter angle subroutine would change the energy of the electron (if scattering mechanism entailed an energy change) and shifts the electron to a new subband if the scattering mechanism caused an *intersubband* scattering.

The magnitude of the electron wavevector kz is then calculated from the new energy according to the non-parabolic E-k relationship. For isotropic mechanisms like acoustic scattering, the direction of the wavevector, forward (+z) or backward (-z), is randomized.

For non-isotropic mechanisms like polar optical phonon scattering or piezoelectric scattering, the direction of the new electron wavevector is chosen according to the mechanism so selected. For example, if a polar optical phonon forward scattering (emission) is selected, then there would be no change in the direction of the electron wavevector, while the direction is reversed if backward scattering is selected.

- Histograms_Mobility

As the name suggests, this subroutine calculates the histograms as well as the ensemble averages of subband velocity and subband energy. The ensemble average of the subband velocity at time-step t for N particles for the n^{th} subband is calculated as

$$v_n^t = \frac{1}{N_n}\sum_{j=1}^{N_n} v_j \tag{4.12}$$

Similarly, at time step t, the mean electron drift velocity is calculated as

$$v_{avg}^t = \frac{1}{m}\sum_{n=1}^{m} v_m^t \tag{4.12}$$

Where m is the total number of subbands in the system.

The mean energy of the electrons at each time step t is calculated in a similar fashion

$$E_n^t = \frac{1}{N_n}\sum_{j=1}^{N_n} E_j \tag{4.13}$$

$$E_{avg}^t = \frac{1}{m}\sum_{n=1}^{m} E_m^t \tag{4.14}$$

Upon reaching steady state, the mobility is calculated by a weighted average of the mobility of each subband, which is in turn calculated by dividing the steady-state subband velocity with the applied field ϵ. Numerically, mobility of the n^{th} subband is calculated as

$$\mu_n = \frac{v_n^{steady\ state}}{\epsilon} \tag{4.13}$$

For M subbands, the weighted average of mobility is calculated as

$$\mu = \frac{\sum_{i=1}^{M} \mu_i N_i}{\sum_{i=1}^{M} N_i} \tag{4.14}$$

Where N_i is the subband population of the i^{th} subband.

The simulation parameters and results are presented in the next chapter.

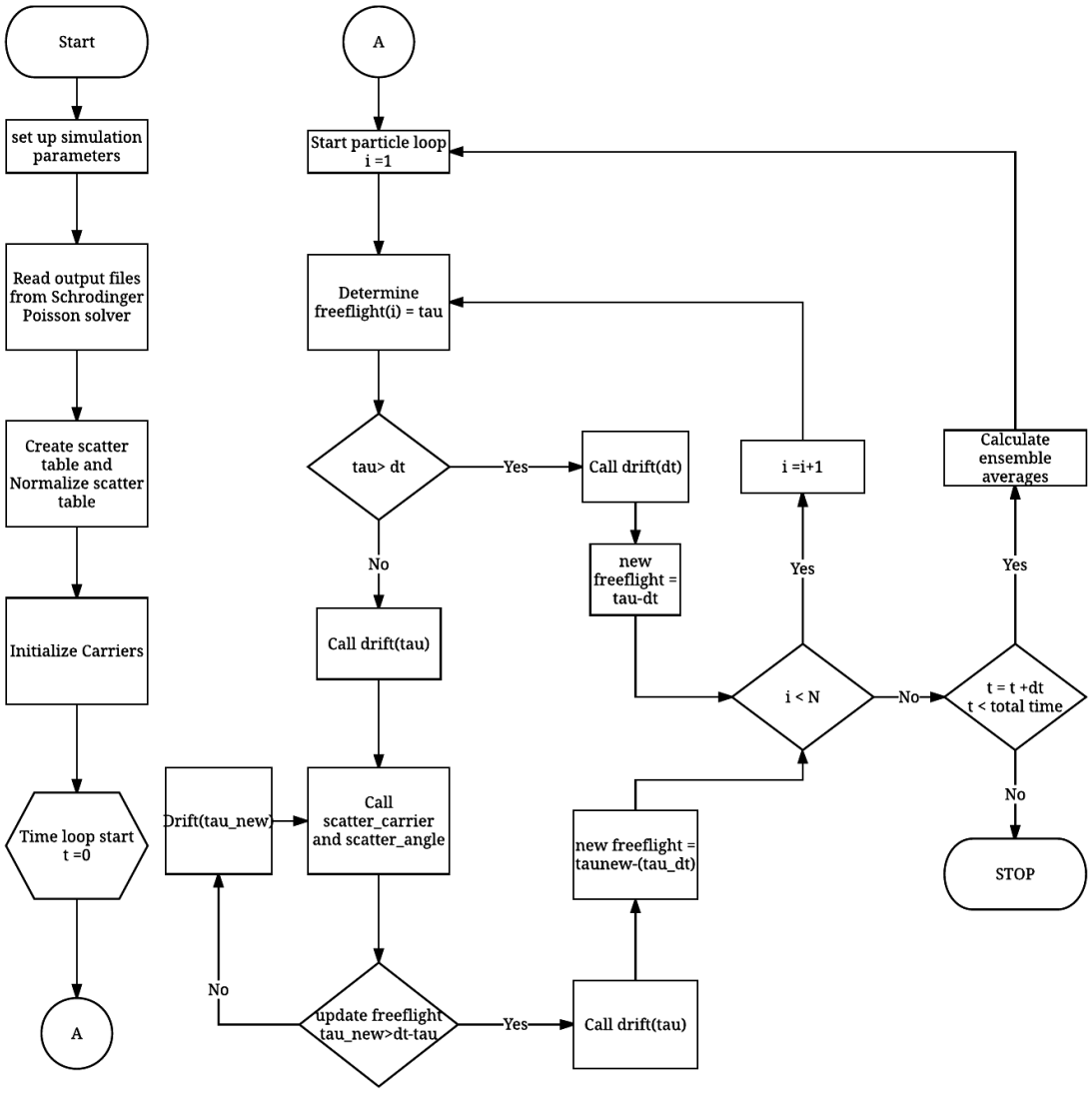

Figure 4.3 The complete 1D Monte Carlo algorithm

CHAPTER 5

STEADY STATE RESULTS

5.1 Simulation Parameters and Program design

The device design is introduced in Chapter 1. The device dimensions along with the mesh spacing is stored in a file and read into the Schrödinger solver at the start of the routine. The program is arranged as follows; Material and device parameters as per Table 5.1 and 5.2 are read into the main program. Gate voltages are applied onto the double gates. The Schrödinger-Poisson solver is then executed. The Monte-Carlo is executed next. The applied field is varied from 1-10 kV/cm and the steady-state results are saved.

Table 5.1 Material Parameters used in Schrodinger Poisson Solver

Parameter	**GaN**	**AlN**	**AlGaN**	**References**
Aluminum Composition	-	-	0.25	
Bandgap (eV)	3.39	6.12	Linearly interpolated	[32]
Effective Mass (Γ1 valley) (m_o)	0.2	0.31	Linearly interpolated	[33]
Electron Affinity (χ) (eV)	3.3	1.64	2.4	[34]
Relative permittivity (ε)	8.9	8.5	Linearly interpolated	[33]
Lattice Constant (Å)	3.189	3.112	Linearly Interpolated	[35]

Table 5.2 Device Dimensions

Parameter	**GaN**	**AlN**	**AlGaN**
Doping (m^{-3})	$5x10^{22}$ n-type	$1x10^{25}$ n-type	$1x10^{24}$ n-type
Layer thickness (nm)	200	8	20
Gate Length (nm)	-	-	100
Nanowire width (nm)	87	-	-
Nanowire thickness(nm)	15	-	-

Table 5.3 Piezoelectric Parameters

Parameter	**GaN**	**AlN**	**AlGaN**	**References**
Spontaneous Polarization (P_{SP}) (C/m^2)	-0.029	-0.081	Linearly interpolated	[12]
$e_{33}(C/m^2)$	0.73	1.46	Linearly Interpolated	[12]
$e_{31}(C/m^2)$	-0.49	-0.60	Linearly Interpolated	[12]
$e_{15}(C/m^2)$	-0.3	-0.48	Linearly Interpolated	[12]
ϵ_{11}	9.5	9.0		[12]
ϵ_{33}	10.4	10.7		[12]
$C_T(Pa)$	$2.65x10^{11}$	-	-	[28]
$C_L(Pa)$	$4.42x10^{10}$			[28]

Table 5.3 highlights the piezoelectric parameters used in calculation of piezoelectric polarization charges for use in the Schrödinger-Poisson solver as well as the piezoelectric scattering rates.

5.2 Schrödinger Poisson Solver Results

In the following figures, both the classical and quantum mechanical results of the Schrödinger-Poisson solver are shown. The dual gates are biased at -3V each to induce creation of channel.

5.2.1 Conduction Band Energy

Figures 5.1-5.3 show the conduction band profile of the device. Figure 5.1 shows a 3D plot of the entire device. The quasi 1D region created is indicated. Figures 5.2 and 5.3 further show the conduction band edge at the AlN/GaN interface as a 2D plot. One can see the creation of wells along the device width (X) and thickness (Y). The zero level is taken as the reference and the Fermi level (E_F). This conduction band profile acts as a confining potential in the Schrodinger Equation solver.

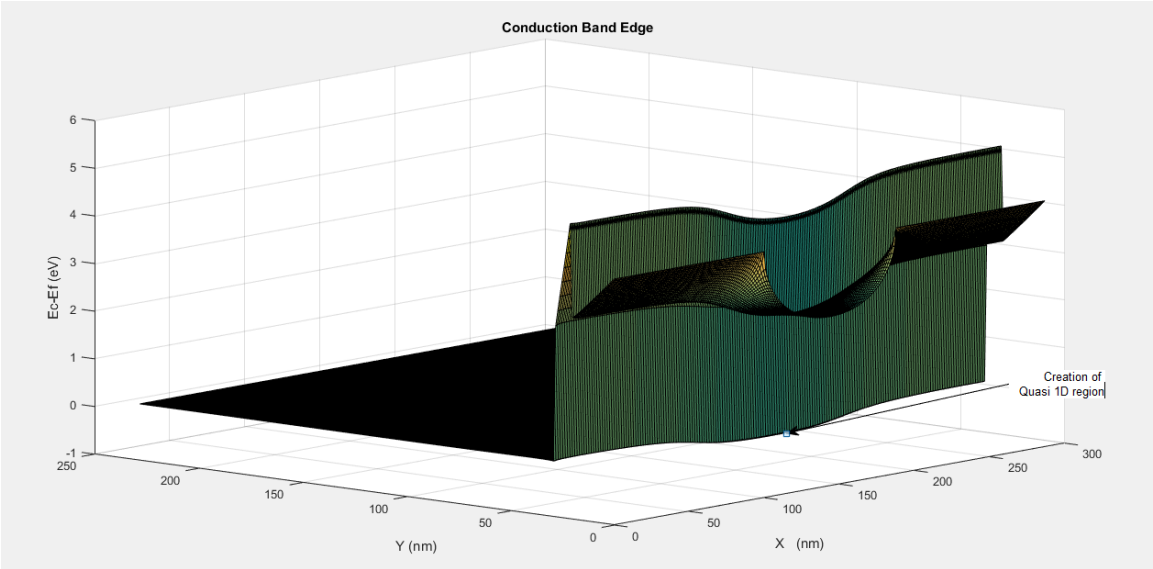

Figure 5.1 3D plot showing the Conduction band energy of the entire device.

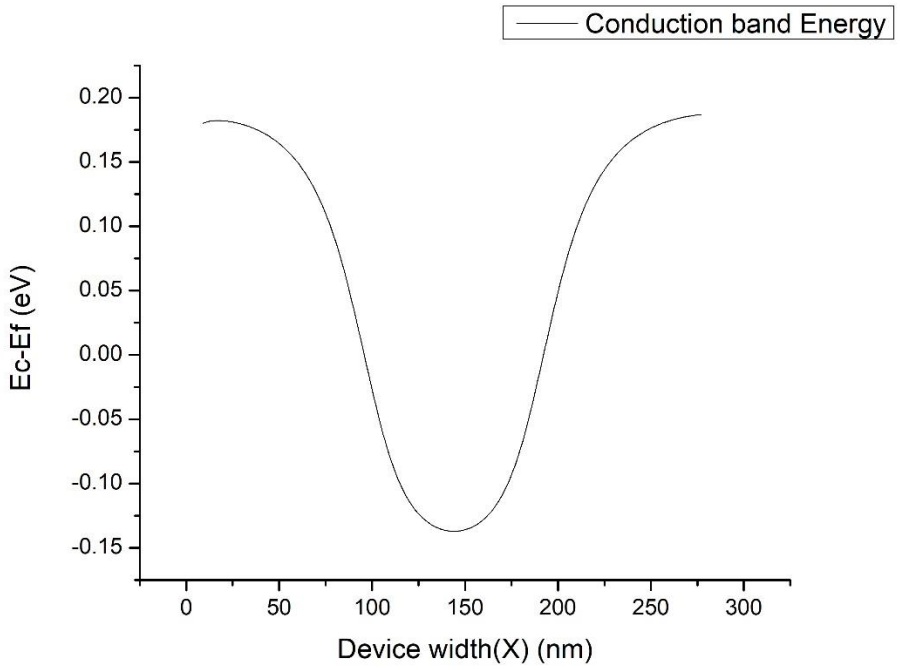

Figure 5.2 Conduction band profile along the width of the device at the AlN/GaN interface.

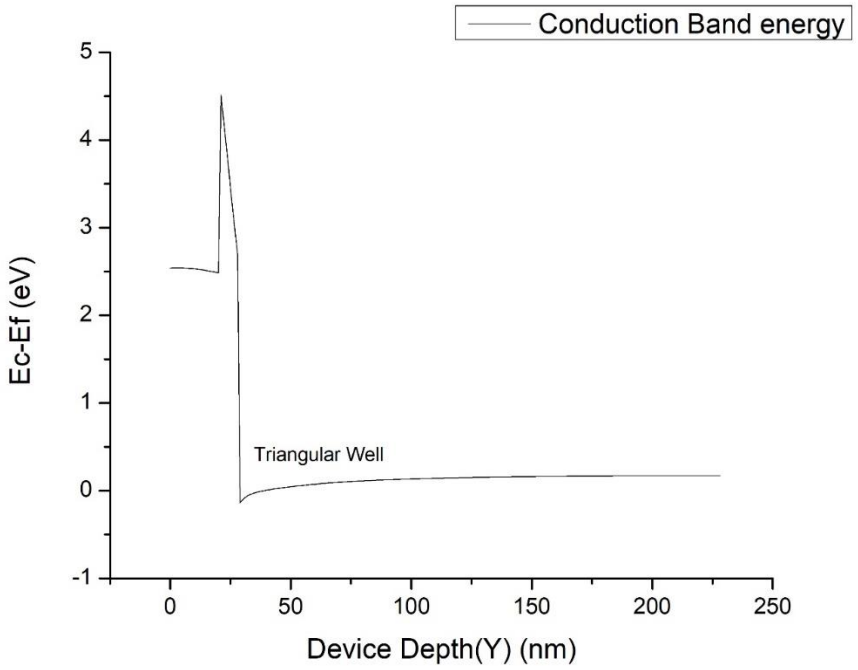

Figure 5.3 Conduction band profile along the depth of the device. The cutline is taken at the center of the well created along the width X.

As seen in figure 5.3, the triangular well is created in GaN layer near the AlN/GaN interface. Seen together, figures 5.2 and 5.3 describe the 2-dimensional potential well created, which forms the quasi-1D nanowire region.

5.2.2 Electron Density

The electron density in the quasi 1D region are plotted below. The electron density is obtained as discussed in Chapter 2 upon solving Schrödinger's equation in the nanowire region self-consistently with Poisson's equation. Figure 5.4 shows a 3D plot of the electron density calculated in the nanowire. As can be seen, the density peaks at the center of the nanowire, below the AlN/GaN interface. Figures 5.5 and 5.6 show the electron density along with the conduction band profile.

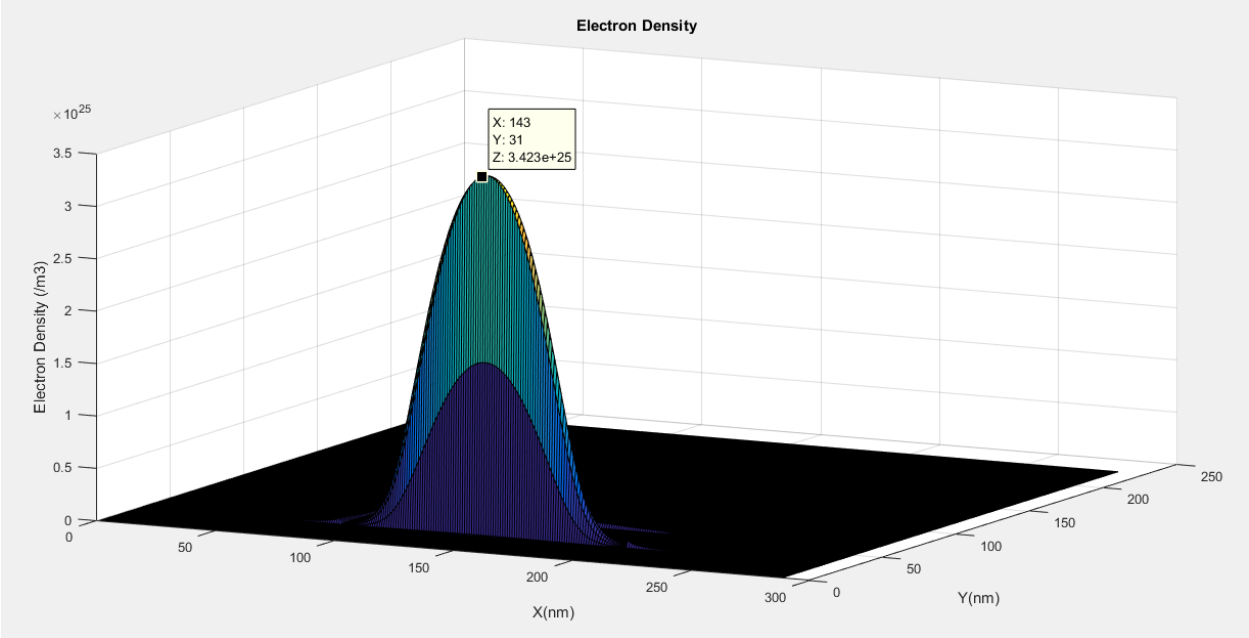

Figure 5.4 Electron Density in the nanowire determined by self-consistent solution of Schrodinger Poisson Equation.

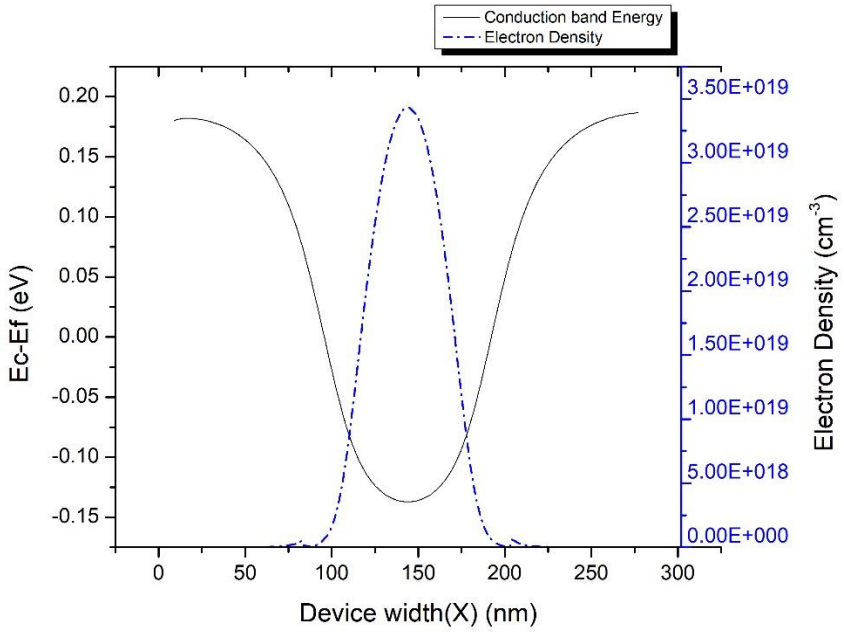

Figure 5.5 Electron density at the interface along device width. The density peaks at x = 144nm, which is the center of the nanowire.

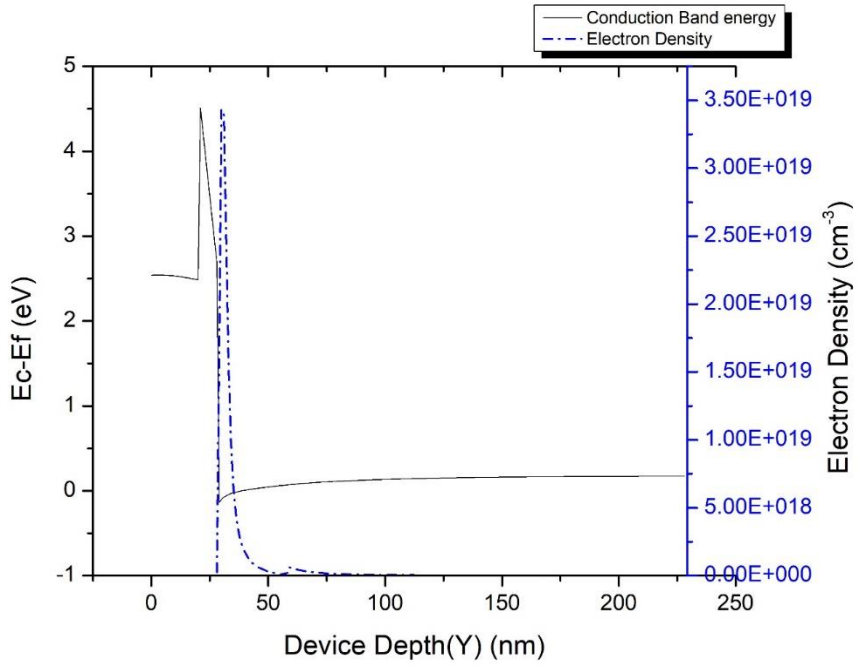

Figure 5.6 Electron density at the center of the nanowire along device depth.

5.2.3 Subband Energies and Wavefunctions

The Schrödinger Solver outputs the eigenvalues and eigenvectors which are used to calculate the subband energies and the subband population in the quasi 1D wire. The eigenvectors are normalized to yield the wavefunctions in the quasi 1D region.

The first 15 eigenvalues were extracted from the eigenvalue solver which form the subband energies of the quasi-1D nanowire. The Subband energies (E_i) and the electron line density in each subband (N_i) is plotted in Figure 5.7.

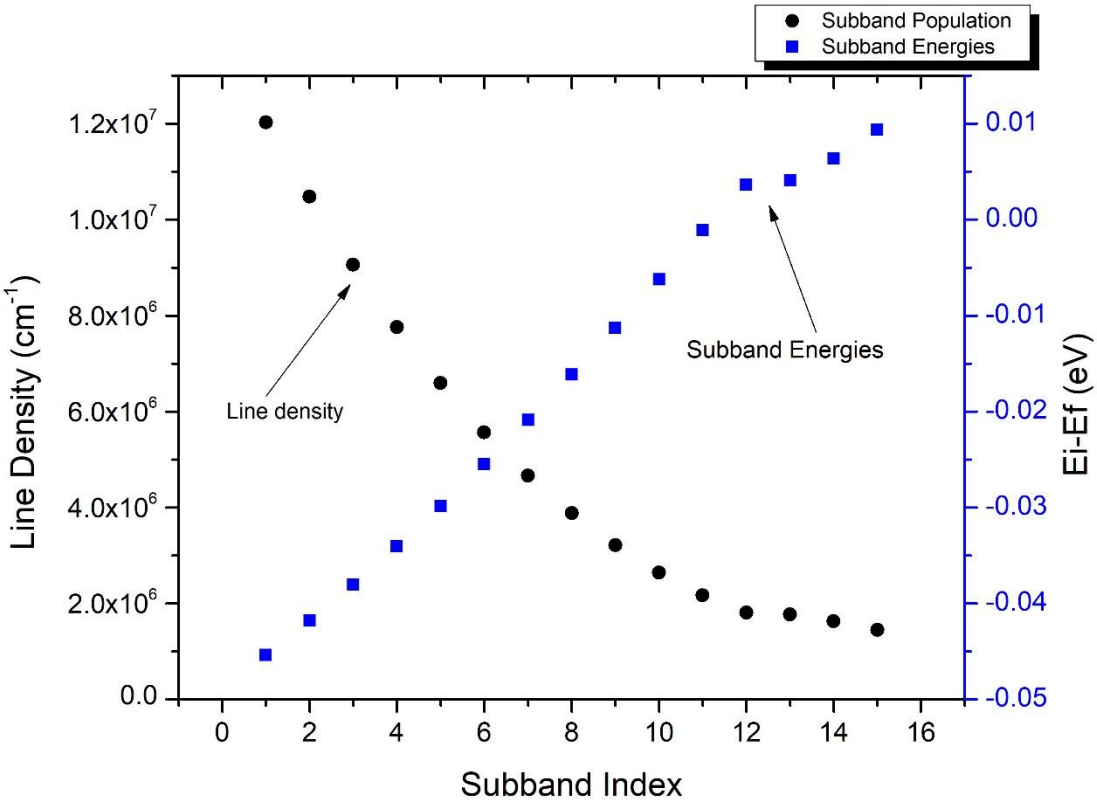

Figure 5.7 Subband Energy (E_i) and population of the first 15 subbands

The wavefunctions are obtained by normalizing the Eigen Vectors. The wavefunctions of the first two subbands are shown in figures 5.8 and 5.9.

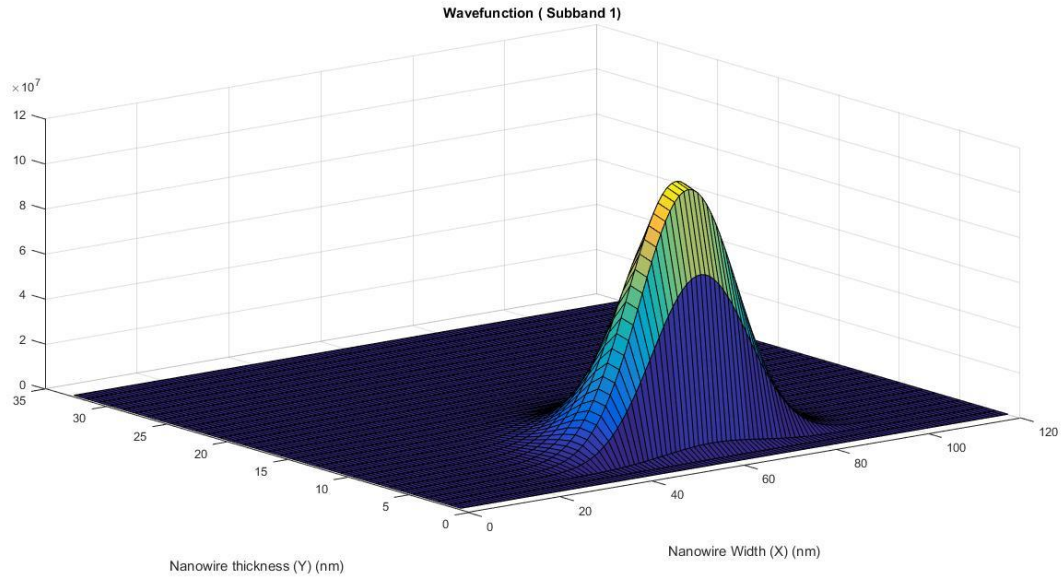

Figure 5.8 Wavefunction for the first energy level (E1)

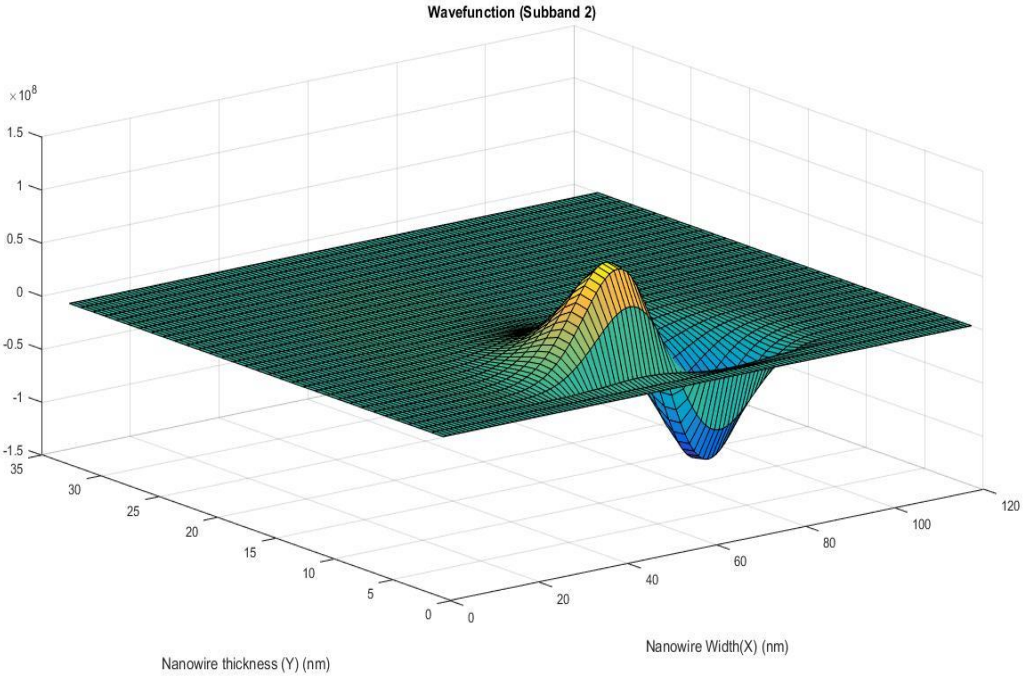

Figure 5.9 Wavefunction for the second energy level (E2)

5.3 Monte Carlo Solver Results

The Monte Carlo solver is built as described in Chapters 3 and 4. Tables 5.4 and 5.5 list the initialization parameters for the Solver. The subband energies and population as well as the wavefunctions are imported from the Schrodinger Solver. The initial distribution of electrons into subbands is done according to the subband population data.

The Monte Carlo simulation domain is the quasi 1D nanowire region. Single valley (Γ1) non-parabolic band structure is adopted for GaN. Since this is a simulation of low-field transport, intervalley scattering is not accounted for in this work.

Table 5.4 Material Parameters (GaN) for Monte Carlo Solver

Parameter	Value	References
Non Parabolicity (α)	0.189 eV	
Effective Mass (m*)	0.2	[32]
Static Dielectric constant (ε_0)	8.9	[32]
High Frequency Dielectric constant (ε_∞)	5.35	[32]
Material Density	6150 Kg/m^3	[36]
Sound Velocity	6560 m/s	[36]
Deformation Potential	8.3 eV	[36]
Optical Phonon energy	0.0912 eV	[36]

Table 5.5 Simulation parameters for Monte Carlo Solver

Parameter	Value
Number of simulation electrons	20000
Step interval	10 fs
Total Simulation time	20 ps
Applied Field (z)	1 kV/cm

5.3.1 Scattering Rates

The following figures show the cumulative scattering rates out of the first subband (n=1) for acoustic scattering, piezoelectric scattering and polar optical phonon (absorption and emission) scattering respectively. The cumulative scattering rate out of subband 'n' for each scattering mechanism is arrived at by totaling the scattering rate (Γ_{nm}) over all the final subbands 'm'.

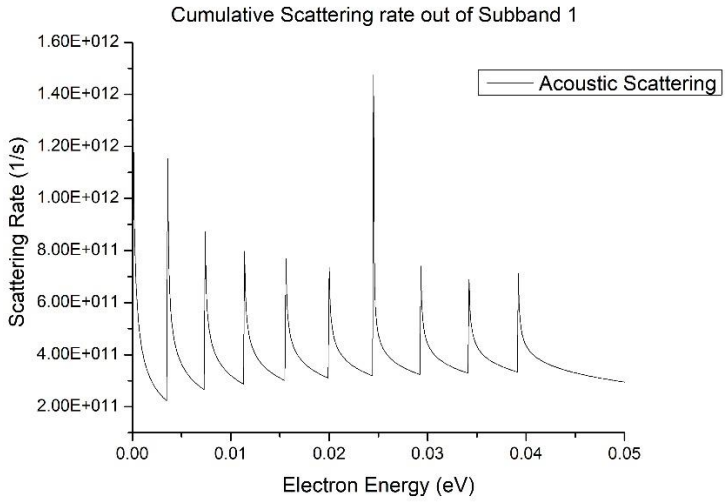

Figure 5.10 Acoustic Scattering rate out of the first subband.

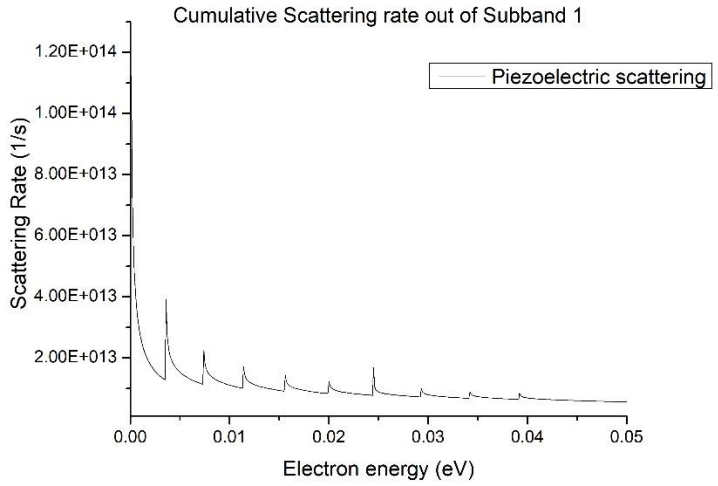

Figure 5.11 Piezoelectric Scattering rate out of the first subband.

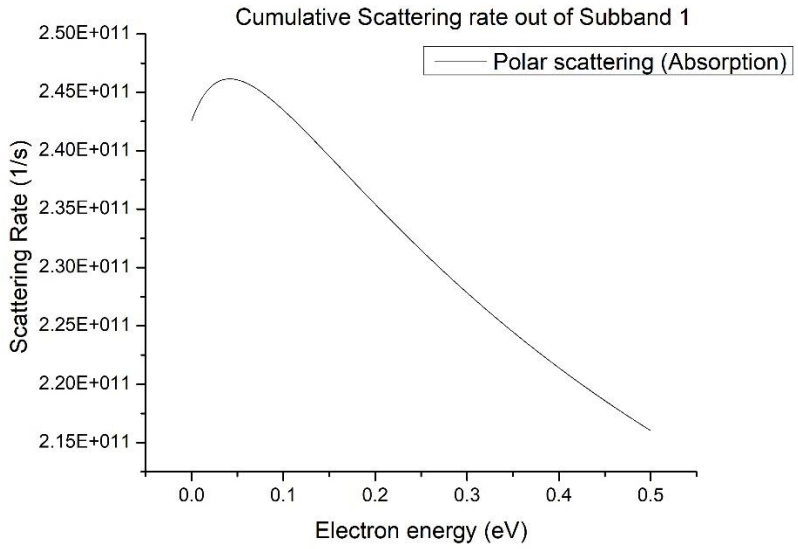

Figure 5.12 Polar optical Absorption Scattering rate out of the first subband.

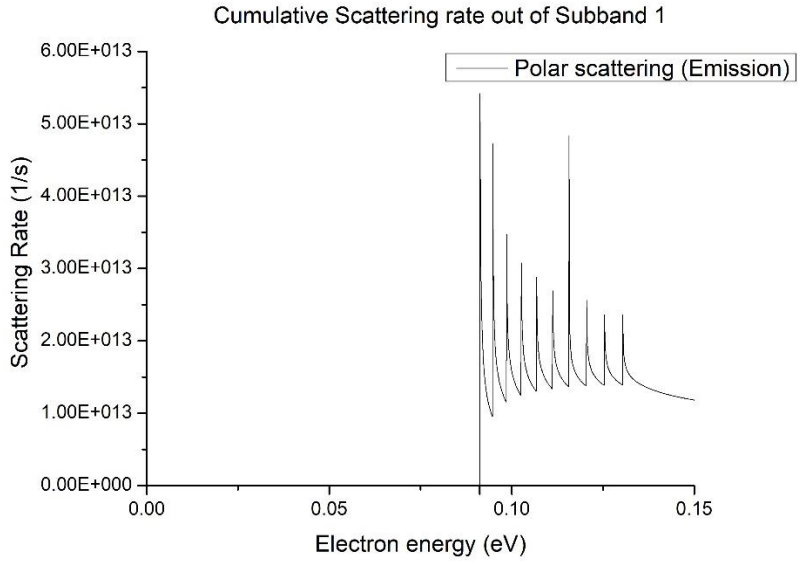

Figure 5.13 Polar optical Emission Scattering rate out of the first subband.

The scattering rates carry the signature of 1D density of states with the peaks being the result of the Heaviside step function which allow *intersubband* scattering only when the kinetic energy of the electron exceeds the difference in subband energy.

Piezoelectric scattering rate behaves similarly to the acoustic scattering rates, due in part to the fact that acoustic phonons are responsible for both. At low energies, the frequency of piezoelectric scattering is much higher than acoustic scattering, leading to the former being a dominant scattering mechanism for low field transport. This is expected since GaN is a highly piezoelectric material.

Out of the two polar optical phonon scattering rates, polar optical phonon emission has a higher scattering rate. But polar optical emission has a threshold energy which is equal to the optical phonon energy, since only upon exceeding this energy the electron can emit an optical phonon. At low fields, the electrons would be unable to gain this energy, hence the Polar optical phonon scattering would not be a dominant mechanism.

5.3.2 Electron distribution, Transient and Steady State results

During initialization, the energy of the electrons is assigned according to Boltzmann distribution. In accordance with the limited degrees of freedom for the electrons (1D) in the confined nanowire, the energy of each electron is assigned as

$$e = -\frac{1}{2}\kappa T \ln r \tag{5.1}$$

here, r is uniformly distributed random number between 0 and 1.

Figures 5.14 and 5.15 plot a histogram of the energy of the carriers after initialization and after the end of simulation respectively.

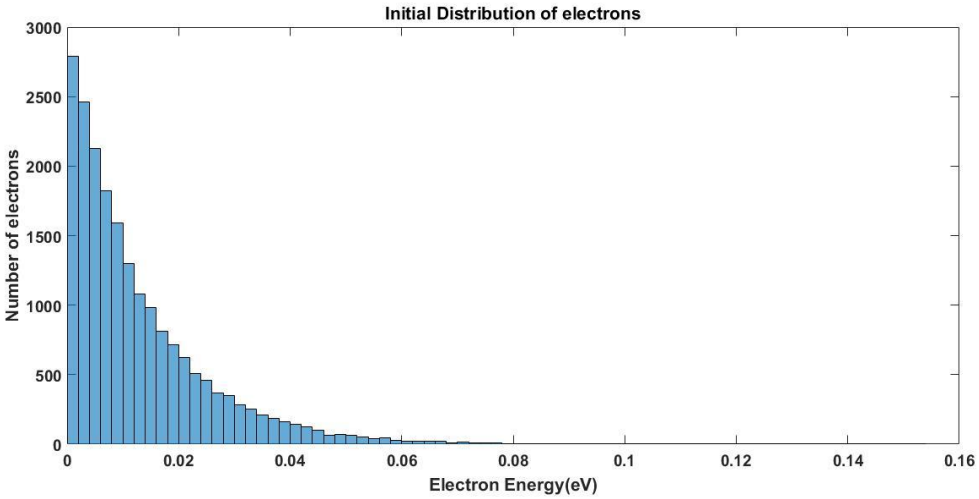

Figure 5.14 The energy of electrons after initialization, plotted as a histogram.

The electron distribution changes as the electrons gain and lose energy by undergoing scattering and drift processes. The changed electron distribution after reaching steady state is shown in figure 5.15 for an applied field of 1kV/cm.

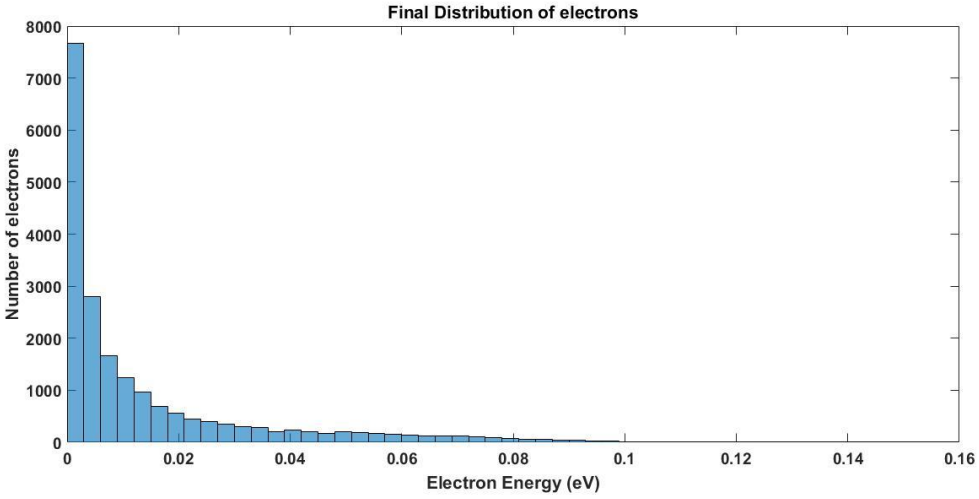

Figure 5.15 Electron energy distribution after reaching steady state for an applied field of 1kV/cm

The transient behavior of the mean electron energy and mean drift velocity, for an applied field of 1kV/cm, is shown in figures 5.16 and 5.17. The figures plot the mean electron

energy and the mean drift velocity, obtained as shown in chapter 4, versus the simulation time. The electron energy rises initially as the electrons gain energy from the applied field and then settles down as they lose the excess energy to scattering processes. At steady state, the mean energy is 16.5 millielectronvolts for an applied field of 1kV/cm.

The drift velocity is negative implying that the electrons are traveling in the opposite direction to the applied field (+z). The transient behavior of mean drift velocity is also similar to that of the mean energy and it reaches a steady state velocity of $v_d = 3.15\times10^6\ cm/s$.

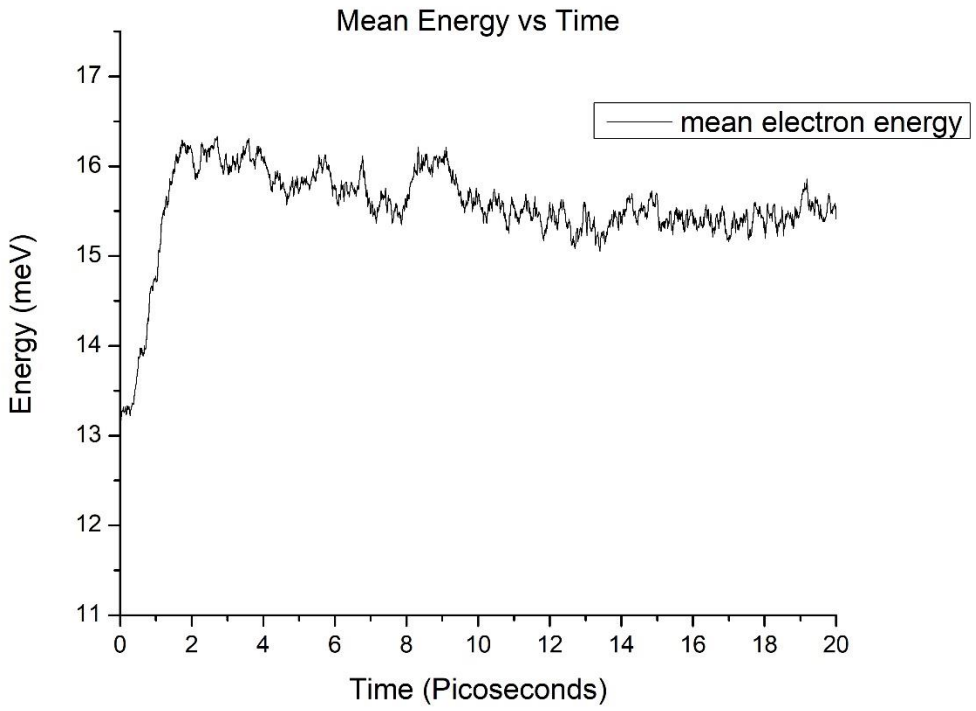

Figure 5.16 Mean electron energy versus time (Applied field 1kV/cm)

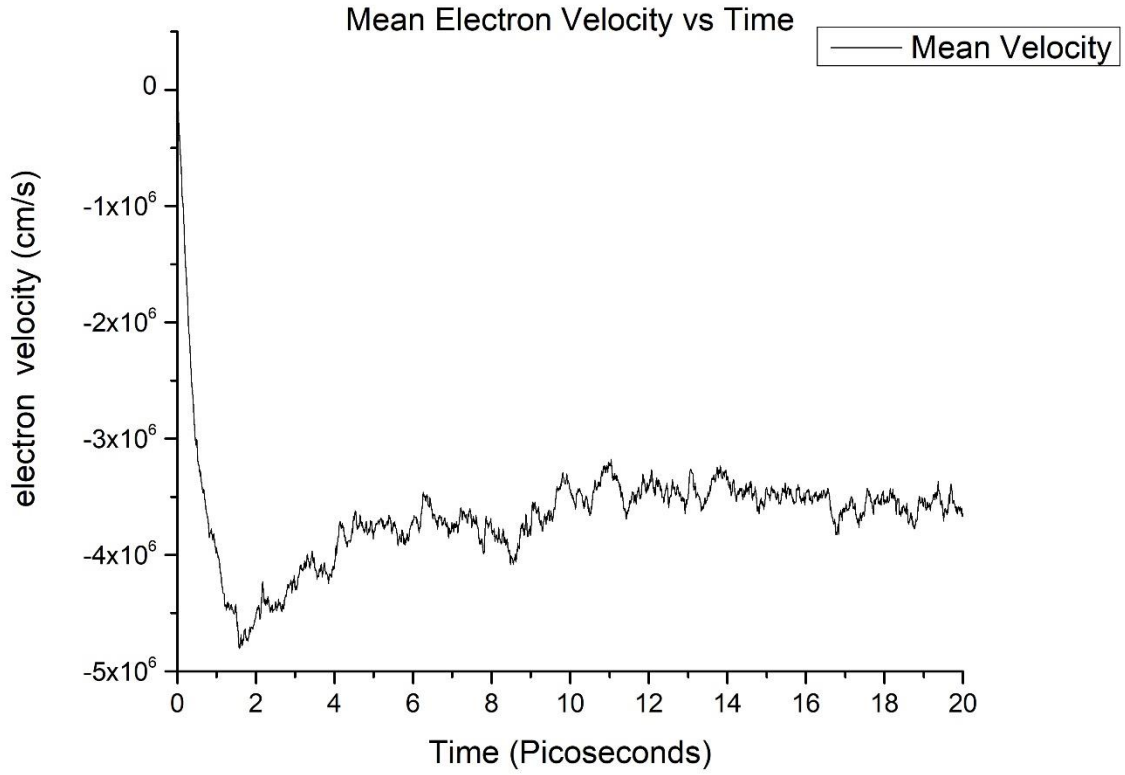

Figure 5.17 Mean electron velocity versus time (Applied field 1kV/cm)

The applied field was varied from 1kV/cm to 10kV/cm and the steady state characteristics was obtained. As the applied field increases, the electron energy increases enabling a higher number of *intersubband* scattering. This alters the subband population and hence the mobility. Figure 5.18 shows the subband population as a function of the applied field. As the magnitude of the applied field increases, intersubband transitions increase which is evident by the decrease in the population of the first subband.

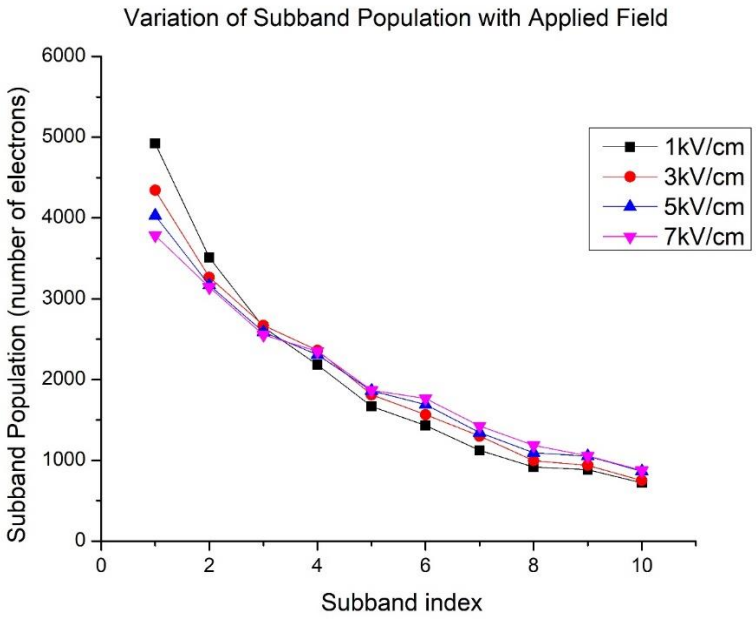

Figure 5.18 Variation of subband population with applied field.

5.4 Mobility Results and Inferences

The electron mobility is calculated by the first calculating the mobility of each individual subband and then averaging it using the subband population as weights. Numerically,

$$\mu = \frac{\sum_{i=1}^{M} \mu_i N_i}{\sum_{i=1}^{M} N_i} \tag{5.2}$$

Table 5.6 shows the calculation process for an applied field of 1 kV/cm. Figure 5.19 shows the Velocity vs field curve for the nanowire. It is seen that in the low field regime (up to 7 kV/cm), the velocity varies linearly with field, hence implying that the mobility remains constant. At fields at and above 10 kV/cm, there is a noticeable increase in the slope of the curve. However, one should note that intervalley scattering mechanisms, which are not considered in this work, may increase at these energies and hence this model may not be accurate.

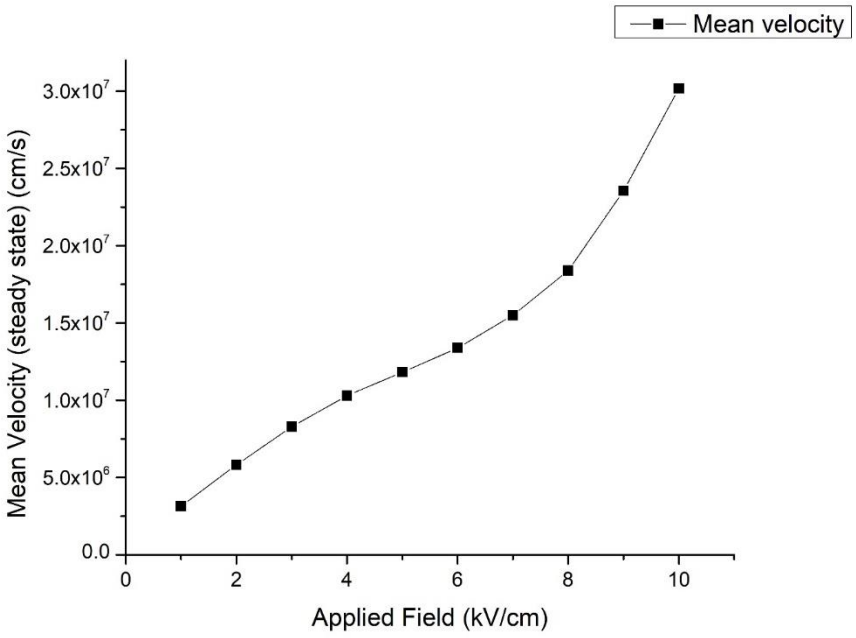

Figure 5.19 Mean electron velocity vs Applied field

Table 5.6 Mobility Calculation for an applied field (ϵ = 1kV/cm)

Subband Velocity (v_i) (m/s)	**Subband Population (n_i)**	$\frac{v_i}{\epsilon} n_i$
23099.72	4922	1.14E+03
27658.43	3510	9.71E+02
28892.77	2646	7.65E+02
29215.7	2181	6.37E+02
36991.53	1667	6.17E+02
38323.75	1432	5.49E+02
39513.04	1122	4.43E+02
45091.28	918	4.14E+02
46425.46	883	4.10E+02
49764.2	719	3.58E+02
Mobility $(\frac{cm^2}{V}.s)$	$\frac{\sum \frac{v_i}{\epsilon} n_i}{\sum n_i}$	**3149.96**

5.4.1 Comments on Mobility and Experimental Validation

The electron mobility of the GaN nanowire considered in this work is determined to be about **3150** $cm^2/V.s$. It should be noted that this is a low field mobility and considers only three electron-phonon scattering mechanisms while leaving out impurity scattering such as Coulomb scattering and Dislocation scattering. Both mechanisms can be a limiting factor to electron mobility. However, since the GaN region is lightly doped, not considering ionized impurity scattering can be justified to an extent.

Indeed, the authors in paper[37] grow a similar AlGaN/AlN/GaN nanowire, albeit with radial geometry) without any doping. They report an intrinsic mobility of **3100** $cm^2/V.s$. at 300K determined through four-probe measurements. Since the as-grown nanowire consisted of intrinsic, high purity GaN, it would be safe to say that the mobility would not be limited by ionized impurity scattering or dislocation scattering. Figure 5.20 shows a snapshot of the experimental structure and the subsequent result.

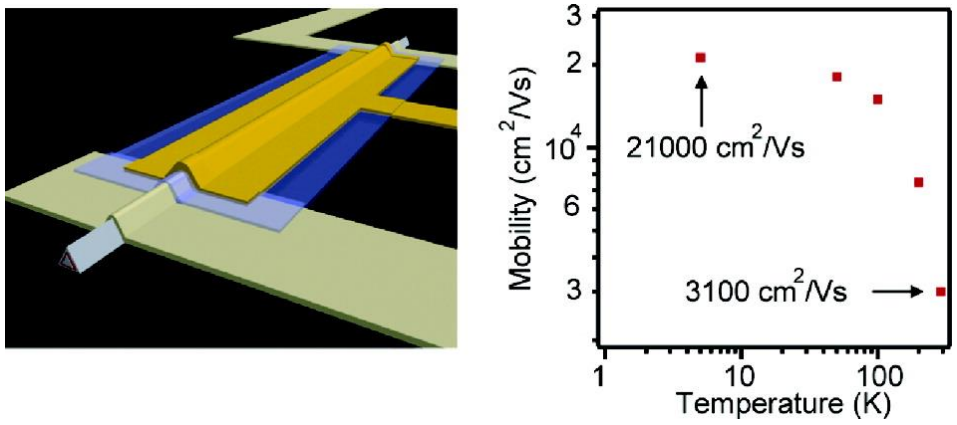

Figure 5.20 The experimental structure and mobility reported by authors in [37]
Figure Courtesy of [37]

As such, the mobility calculated in this work closely matches the experimental mobility obtained for a similar structure, validating the model and solver used in this work. Since

the solver developed in this work is generic, further scattering mechanisms can be conveniently added as and when needed.

The dominant scattering mechanism in the low field regime is found to be Piezoelectric scattering. As can be seen in figures 5.14 and 5.15, mean energy of the electrons is not enough to activate polar optical phonon scattering. However, as the applied field is increased, Polar optical scattering becomes increasingly dominant as a higher number of electrons gain excess energy over the optical phonon energy. This also means that due to the high optical phonon energy in GaN, the electrons have fewer scattering mechanisms at very low fields, paving the way for GaN nanowires to be used in applications such as ballistic transport.

CHAPTER 6

CONCLUSION AND FUTURE WORK

6.1 Conclusion

Semiconductor nanowires are finding a variety of application from logic devices and FETs to solar cells. The attractive properties of gallium nitride make it a potential candidate for many nanowire applications and hence the need to develop a mobility model arises. This work developed a low field mobility model for AlGaN/GaN Heterostructure nanowires. A 2 dimensional self-consistent Schrödinger-Poisson solver was developed and coupled with a 1 dimensional Monte Carlo solver.

Two-dimensional confinement was achieved by designing a double gated $Al_{0.25}Ga_{0.75}N$/AlN/GaN Heterostructure with 20 nm thick AlGaN and 8 nm thick AlN layers. The triangular and square wells so formed created a quasi 1D nanowire region.

The self-consistent Schrödinger-Poisson solver determined the subband energies and the respective line densities as well as the electron wavefunctions which were in turn fed to the Monte Carlo solver. Three electron phonon scattering mechanisms were considered: acoustic phonon scattering, polar optical phonon scattering and piezoelectric scattering. Expressions for the one-dimensional scattering rates were derived for all three. The scattering rates were determined to be a strong function of the overlap integrals between the initial and the final states. These were obtained by coupling the wavefunctions of the initial and final electronic states.

The one-dimensional Monte Carlo kernel was operated on the quasi 1D nanowire region and steady state results were obtained. The velocity vs. field characteristics were obtained for the low field regime by varying the applied fields in the 1kV/cm-10 kV/cm range. The

resulting characteristics suggested a linear Velocity variation vs. field in the low field regime.

The electron mobility was determined to be **3150 cm^2/V-s** which agrees with experimental results for intrinsic mobility of an undoped GaN nanowire. Among the scattering mechanisms considered, piezoelectric scattering was found to be most dominant at low fields. As expected, since the polar optical phonon is very high for GaN, the electrons do not scatter from polar optical phonons.

6.2 Future Directions of Research

- Scattering Mechanisms

Further scattering mechanisms such as impurity scattering may be added to accurately model highly doped nanowires. Interface roughness scattering can be added to account for scattering at the GaN/AlGaN hetero-interface. Dislocation scattering mechanism may also be necessary to account for scattering from dislocation cores arising due to dislocations present in the crystal.

- Coupled Schrodinger - Monte Carlo Solver (Device Simulation)

The Schrodinger-Poisson solver can be solved in slices and coupled with Monte Carlo device solver to simulate I-V characteristics of a device.

- Confined Phonons

The confinement of phonons was not considered in this work. The impact of spatial confinement of phonons on the electron mobility may become noticeable in dimensions below 10 nm. Further research is necessary to account for confined phonons.

- Investigation of some novel applications

Many applications for nanowires discussed in this work such as a Nanowire FET or a Ballistic transport device may be investigated by extending this solver.

- Collisional Broadening of states and Green's function solver

A full quantum-mechanical treatment of GaN nanowires would entail accounting for the collisional broadening of the states and designing a Green's function solver for mobility calculation in nanowires.

REFERENCES

[1] S. N. Mohammad, “Quantum-confined nanowires as vehicles for enhanced electrical transport.,” *Nanotechnology*, vol. 23, no. 28, p. 285707, 2012.

[2] M. Mongillo, P. Spathis, G. Katsaros, P. Gentile, and S. De Franceschi, “Multifunctional devices and logic gates with undoped silicon nanowires,” *Nano Lett.*, vol. 12, no. 6, pp. 3074–3079, 2012.

[3] U. Chatterjee, J. H. Park, D. Y. Um, and C. R. Lee, “III-nitride nanowires for solar light harvesting: A review,” *Renew. Sustain. Energy Rev.*, vol. 79, no. June 2016, pp. 1002–1015, 2017.

[4] U. Semiconductors, “Ultrawide - Bandgap Semiconductors : Research Opportunities and Challenges,” 2016.

[5] S. M. Galagali, N. S. Sankeshwar, and B. G. Mulimani, “Piezoelectric phonon-limited electron mobility in GaN nanowires,” vol. 1, no. 4, pp. 460–463, 2013.

[6] Y. Huang, X. Duan, Y. Cui, and C. M. Lieber, “Gallium Nitride Nanowire Nanodevices,” *Nano Lett.*, vol. 2, no. 2, pp. 101–104, 2002.

[7] E. Matioli, “Room-Temperature Ballistic Transport in III-Nitride Heterostructures,” 2015.

[8] G. Suo, S. Jiang, J. Zhang, J. Li, and M. He, “GaN Nanowires,” vol. 2014, no. 1, 2014.

[9] G. Santoruvo, A. Allain, D. Ovchinnikov, and E. Matioli, “Magneto-ballistic transport in GaN nanowires,” *Appl. Phys. Lett.*, vol. 109, no. 10, 2016.

[10] F. Bernardini, V. Fiorentini, and D. Vanderbilt, “Spontaneous polarization and piezoelectric constants of III-V nitrides,” vol. 56, no. 16, pp. 24–27, 1997.

[11] B. Padmanabhan, “Modeling Reliability of Gallium Nitride High Electron Mobility Transistors,” Arizona State University, 2013.

[12] O. Ambacher *et al.*, “Two dimensional electron gases induced by spontaneous and piezoelectric polarization in undoped and doped AlGaN/GaN heterostructures,” *J. Appl. Phys.*, vol. 87, no. 1, pp. 334–344, 2000.

[13] R. F. Pierret, “Semiconductor Device Fundamentals,” *New York*, p. 792, 1996.

[14] S. R. Mehrotra, L. K. Zentner, G. Klimeck, and D. Vasileska, “NanoHUB.org - The ABACUS tool suite as a framework for semiconductor education courses,” in *Proceedings of the IEEE Conference on Nanotechnology*, 2011, pp. 932–936.

[15] D. M. J. Young, “Iterative Methods for Solving Partial Difference Equations of Rlliptical Type,” p. 74, 1950.

[16] “Maxwell / Poisson Equation Solvers Coupling of Transport Equations to Poisson and Band-Structure Solvers.”

[17] E. B. R. I. Knezevic, “Self-consistent Poisson-Schrödinger-Monte Carlo solver : electron mobility in silicon nanowires,” pp. 206–210, 2010.

[18] U. Ravaioli, “Introduction to Quantum Models,” vol. 0, no. 6, pp. 1–17.

[19] “LAPACK.” [Online]. Available: http://netlib.org.

[20] X. Aymerich-Humet, F. Serra-Mestres, and J. Millán, “A generalized approximation of the Fermi-Dirac integrals,” *J. Appl. Phys.*, vol. 54, no. 5, pp. 2850–2851, 1983.

[21] M. Lundstrom, “Heterostructure Fundamentals Notes.” Purdue University, p. 43, 1995.

[22] D. Vasileska, “Confined Carriers-Scattering Rates Calculation.” [Online]. Available: https://nanohub.org/resources/11530.

[23] D. Vasileska, “Scattering Rates for Q2D systems.” [Online]. Available: https://nanohub.org/resources/11532.

[24] D. Vasileska and S. M. Goodnick, *Computational Electronics : Semiclassical and quantum device modeling and simulation*, vol. 1, no. 1. 2006.

[25] A. H. Davoody, E. B. Ramayya, L. N. Maurer, and I. Knezevic, “Ultrathin GaN nanowires: Electronic, thermal, and thermoelectric properties,” *Phys. Rev. B - Condens. Matter Mater. Phys.*, vol. 89, no. 11, 2014.

[26] E. B. Ramayya, “M.S Thesis,” Arizona State University, 2005.

[27] M. V Fischetti, “Part IV : Scattering and Interactions,” pp. 203–271, 2010.

[28] S. Yamakawa, R. Akis, N. Faralli, M. Saraniti, and S. M. Goodnick, “Rigid ion model of high field transport in GaN.,” *J. Phys. Condens. Matter*, vol. 21, no. 17, p. 174206, 2009.

[29] D. Vasileska, “Polar Optical Phonon Scattering.” [Online]. Available: https://nanohub.org/resources/11522.

[30] D. Vasileska, “Piezoelectric Scattering Lecture Notes.” [Online]. Available: https://nanohub.org/resources/11524.

[31] R. Hathwar and D. Vasileska, “Generalized Monte Carlo Tool for Investigating

Low-Field and High Field Properties of Materials Using Non-parabolic Band Structure Model," no. June, 2011.

[32] I. Martynova *et al.*, *Materials for electronic devices.*, vol. 423, no. DE102010033548A1. 2012.

[33] V. Bougrov, M. E. Levinshtein, S. L. Rumyantsev, and A. S. Zubrilov, "Gallium Nitride (GaN)," in *Properties of Advanced Semiconductor Materials: GaN, AIN, InN, BN, SiC, SiGe*, 2001, p. 216.

[34] S. P. Grabowski *et al.*, "Electron affinity of AlxGa1-xN(0001) surfaces," *Appl. Phys. Lett.*, vol. 78, no. 17, pp. 2503–2505, 2001.

[35] O. Lagerstedt and B. Monemar, "Variation of lattice parameters in GaN with stoichiometry and doping," *Phys. Rev. B*, vol. 19, no. 6, pp. 3064–3070, 1979.

[36] F. M. A. El-Ela and A. Z. Mohamed, "Temperature and Doping Dependencies of the Transport Properties within GaN and GaAs," *J. Mod. Phys.*, vol. 2, no. 11, pp. 1324–1330, 2011.

[37] Y. Li *et al.*, "Dopant-free GaN/AlN/AlGaN radial nanowire heterostructures as high electron mobility transistors," *Nano Lett.*, vol. 6, no. 7, pp. 1468–1473, 2006.